Materials Advances

ROYAL SOCIETY OF CHEMISTRY

PAPER

View Article Online
View Journal | View Issue

Cite this: *Mater. Adv.*, 2025, **6**, 9064

Integrated experimental and computational investigation of a dual-functional colorimetric probe with anticancer activity for selective arginine sensing: insights from DFT, molecular docking, and molecular dynamics simulations†

Aayushi Joshi,[a] Nikunjkumar Vagadiya,[a] Nisarg Rana,[a] Giftson J. Senapathy,[b] Rakesh Rawal,[c] Helly Shah,[de] Ranjitsinh Devkar,[de] Nandini Mukherjee*[f] and Anu Manhas *[a]

A novel anthracene-based Schiff base probe (**P1**) was synthesized through a facile condensation reaction between an aldehyde and hydrazine hydrate. The resulting compound exhibited exceptional sensitivity and selectivity as a colorimetric chemosensor for arginine detection, with a detection limit of 1.24 nM. Binding stoichiometry and interaction mechanisms were elucidated *via* UV-Vis spectroscopy, while ^{1}H NMR titration experiments supported the proposed binding model. Density functional theory studies, including potential energy surface, electrostatic potential, and non-covalent interaction analyses, further corroborated the interaction. These investigations revealed that the optical response of **P1** arises from an intramolecular charge transfer mechanism, as confirmed by frontier molecular orbital analysis. Importantly, **P1** exhibited promising real-world applicability by successfully detecting arginine in commercial dietary supplements. In addition to its sensing capabilities, **P1** demonstrated notable anticancer activity with an IC_{50} value of 20 μM in MCF7 and HeLa cells, indicating its potential therapeutic utility. The Annexin V–PI data revealed a dose-responsive apoptotic effect by **P1** on cancer cells. Molecular docking studies further revealed a significant binding affinity of **P1** towards the anti-apoptotic protein Myeloid Cell Leukemia 1 (Mcl-1). This stability was further confirmed *via* molecular dynamics simulation studies of the 5FC4_**P1** complex. Moreover, the haemolysis assay results confirmed that **P1** exhibits excellent biocompatibility, further supporting its safety and applicability in therapeutic contexts. These findings suggest that **P1** may serve as a dual-function agent with both diagnostic and therapeutic potential in biomedical applications.

Received 27th June 2025,
Accepted 3rd October 2025

DOI: 10.1039/d5ma00683j

rsc.li/materials-advances

1. Introduction

Amino acids are the fundamental building blocks involved in protein and enzyme synthesis, metabolism, and various cellular processes, making them irreplaceable in biological systems. Among them, arginine plays a pivotal role in several physiological processes, including immune protection,[1] facilitates nutrient transport for metabolic balance, and aids in protein synthesis for tissue repair.[2] Due to its high isoelectric point (pI = 10.76) and strong alkalinity ($pK_a \sim 12.5$), arginine serves as a biochemical precursor for the synthesis of nitric oxide, urea, agmatine, and ornithine.[3] Its guanidinium group remains positively charged under physiological conditions, enabling strong electrostatic interactions with negatively charged biomolecules and enzymes, thereby stabilizing reaction intermediates.[4,5] It also plays a pivotal role in several biological

[a] *Department of Chemistry, Pandit Deendayal Energy University, Gandhinagar, 382426, India. E-mail: anu.manhas15@gmail.com*
[b] *Department of Biotechnology, Pandit Deendayal Energy University, Gandhinagar, 382426, India*
[c] *Department of Medical Biotechnology, Gujarat Biotechnology University, Gandhinagar, India*
[d] *Dr. Vikram Sarabhai Institute of Cell & Molecular Biology, Faculty of Science, The Maharaja Sayajirao University of Baroda, Vadodara, India*
[e] *Department of Zoology, Faculty of Science, The Maharaja Sayajirao University of Baroda, Vadodara, India*
[f] *Department of Chemistry, Dinhata College, West Bengal, India. E-mail: nandini.81129@gmail.com*

† The authors dedicate this work to the memory of Professor Manoj Pandey, who passed away on 27th May, 2025. His constant encouragement, insightful discussions, and unwavering support inspired and motivated us throughout this research. He will be remembered with deep respect and gratitude.

processes, like intestinal stem cell migration, protein regeneration, and cell division.[6] Aberrant levels of arginine are often associated with various disorders, such as cancer, where it contributes to tumor growth and progression through metabolic reprogramming and immune modulation.[7,8] Due to its importance in biological processes, the selective and sensitive detection of arginine in biological systems is of considerable interest for diagnostic and therapeutic applications. To date, numerous methods for arginine detection have been reported in the literature, like fluorescence spectroscopy,[9] electrophoresis,[10] and high-performance liquid chromatography (HPLC).[11] But these methods require laboratory setups, which have limitations for real-time analysis of arginine samples. Therefore, developing a highly selective and fast-responsive probe continues to be of significant interest. In this context, we report a novel colorimetric responsive probe, **P1**, designed to detect arginine with high specificity.

Colorimetric sensors are highly practical, low-cost tools for rapid diagnostics, especially in resource-limited settings.[12] In this context, anthracene is a highly promising scaffold for the development of multifunctional molecules with both sensing and therapeutic capabilities. It possesses unique structural and photophysical properties, such as strong fluorescence, an extended conjugated π-system, and the ability to engage in π–π stacking interactions, all of which are critical for effective sensing and biological activity.[13] Anthracene is a widely utilized fluorophore in the development of chemosensors, owing to its high quantum yield, excellent chemical stability, and ease of structural modification.[14] Moreover, the presence of an aldehyde group in anthracene carbaldehyde allows Schiff base formation, enabling chemical modification for selective sensing, particularly of biomolecules like arginine. Amino acid arginine possesses a unique side chain with a strong hydrogen bonding capacity, high pK_a, and possibility for non-covalent electrostatic interactions. Anthracene's structural features also support DNA intercalation, a well-documented mechanism for the anticancer activity of various drugs.[15] For example, Bisantrene, a modified anthracene derivative, exerts anticancer effects by intercalating into DNA and disrupting key cellular processes.[16] Moreover, certain anthracene-based scaffolds have shown ability to inhibit fat mass and obesity-associated protein, thereby modulating gene expression at the epitranscriptomic level, a distinct and emerging therapeutic strategy.[17] Various fluorescent and colorimetric probes for arginine detection have been reported in recent literature, particularly those based on chiral BINOL (2,2′-dihydroxy-1,1′-binaphthyl) scaffolds. In this respect, a BINOL-based fluorescent sensor was reported for the selective detection of both arginine and lysine with detection limits of 13.07 nM and 12.53 nM, respectively, along with its biocompatibility for cell imaging applications.[18] Similarly, another BINOL-derived probe exhibited specific detection ability of both D-arginine and D-glutamate at low concentrations in food samples, extending its utility to paper-based sensors.[19] The selective detection of arginine alone has been achieved using chiral BINOL-based probes.[20,21] Apart from arginine detection, these probes are also used for D-histidine detection[22]. Overall, these studies explain the progress in the design of chemoselective probes for amino acid detection. Considering the same, the present work focuses on introducing a structurally distinct anthracene-based Schiff base probe (**P1**) that offers dual functionality as a selective colorimetric sensor for arginine and as a potential anticancer agent.

In this study, we report the design, synthesis, and characterization of a new bifunctional colorimetric probe tailored for the selective detection of arginine and evaluation of cytotoxic activity against cancer cells. The probe integrates a responsive chromophoric unit for real-time visual sensing with structural features conducive to biological interaction. Density functional theory (DFT) calculations were performed to gain a better understanding of the amino acid sensing mechanism of the synthesized probe (**P1**). Electronic structure properties were studied using structure optimization, energy calculations, charge analysis, potential energy scanning plots (PES), electrostatic potentials (ESP), and frontier molecular orbital (FMO) analysis. Moreover, natural bond order (NBO) analysis, reduced density gradient (RDG), and non-covalent interaction (NCI) were performed specifically to investigate the hydrogen bonds and other non-covalent interactions. These findings not only corroborate the experimental results but also offer a foundation for the future design of advanced multifunctional molecular sensors. To investigate its therapeutic efficiency, the synthesized compound **P1** was docked in the Mcl-1 protein predicted by the freely available web resource, PASS online, to further evaluate its potential biological activity as an antitumor agent (**https://www.way2drug.com/passonline**). After predicting the biological activity using PASS online and performing docking studies with the target protein, the compound was also subjected to MTT and haemolytic assays to assess its practical application and cytocompatibility. The docked molecule, along with the reference, was subjected to molecular dynamics simulations of 300 ns to investigate the stability of the complex in a biological environment.

2. Materials and methods

Reagents and solvents used for synthesis were of analytical grade. For the UV-Vis studies, spectroscopic-grade solvents were used. Anthracene-9-carbaldehyde and hydrazine hydrate were obtained from Sigma-Aldrich (Merck), while all amino acids were sourced from Spectrochem, Otto Chemie Pvt. Ltd, and Sigma-Aldrich, and were used without further purification. The ^{1}H NMR spectra were recorded at room temperature using a JNM ECZL 400S spectrometer (JEOL, Japan), with tetramethylsilane (TMS) as the internal standard. Chemical shift values are reported in parts per million (ppm). FTIR measurements were performed using a PerkinElmer Affinity FTIR spectrophotometer. The UV-Vis absorption spectra were measured using a Lab India UV-Vis 3000+ spectrophotometer with a quartz cuvette of 1 cm path length. All experiments were carried out in accordance with the compliance standards of the relevant laws and guidelines set by the Indian Medical Association (IMA)

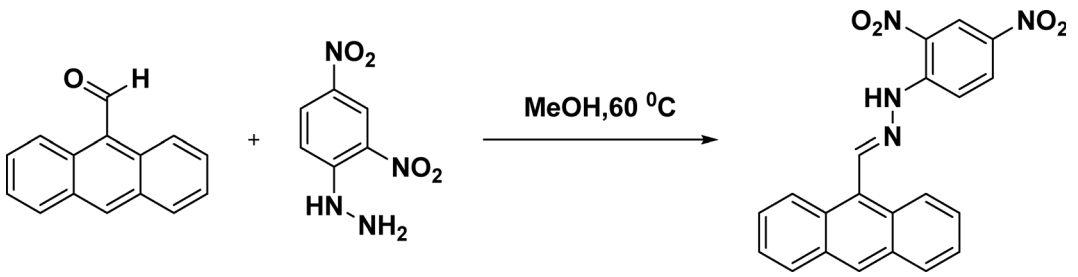

Scheme 1 Synthesis of probe **P1**.

for research involving human subjects. For the haemolysis assay, whole blood was collected from a healthy individual into EDTA-coated vacutainer tubes after obtaining prior informed consent. The experimental protocol received approval from the IMA and was conducted in accordance with ethical guidelines for human subject research at Blue Cross Pathology Lab (IMA-BMWMC No. 1093), Vadodara, India.[23]

2.1. Synthesis of (*E*)-1-(anthracen-9-ylmethylene)-2-(2,4-dinitrophenyl)hydrazine (P1)

To a solution of 9-anthracene carbaldehyde (1 g, 4.84 mmol) in methanol, 2,4-dinitrophenylhydrazine hydrate (1.506 g, 5.33 mmol) was added and refluxed at 60 °C (Scheme 1). The starting material was fully consumed, and the reaction was monitored using TLC. After cooling the reaction mixture, the resultant precipitate was filtered and washed with cold methanol. The crude product was recrystallized with dichloromethane (DCM) to obtain the product as a red solid in 92% yield.

^{1}H-NMR (400 MHz, DMSO-D_6) δ 12.10 (s, 1H) 9.97 (s, 1H) 8.93 (d, J = 2.7 Hz, 1H), 8.81 (d, J = 9.0 Hz, 2H), 8.77 (s, 1H), 8.44 (dd, J = 9.7, 2.7 Hz, 1H), 8.18(d, J = 8.2 Hz, 2H), 8.04 (d, J = 9.5 Hz, 1H), 7.70–7.66 (m, 2H), 7.62–7.59 (m, 2H), HRMS (*m*/*z*): calculated for $C_{21}H_{14}N_4O_4$ $[M+H]^+$ 386.10; found 386.4 (Fig. S1).

2.2. UV-Vis spectroscopic studies

UV-Vis spectroscopy was employed to investigate the interactions between probe **P1** and various amino acids. A stock solution of the 1 mM probe was prepared using spectroscopic-grade DMSO. Stock solutions of 1 mM amino acids, such as alanine, arginine, asparagine, aspartic acid, cysteine, glutamic acid, glutamine, glycine, histidine, isoleucine, leucine, lysine, methionine, phenylalanine, serine, proline, tyrosine, tryptophan, threonine, and valine and the structural homolog ornithine were prepared in double-distilled water. For the binding study, 300 μL of the 1 mM probe solution and 2400 μL of DMSO were combined in a quartz cuvette, followed by the addition of 1 mM analyte solution. The absorption spectra were measured for the probe in the absence and in the presence of the selected amino acids and ornithine to evaluate the interaction dynamics. UV-Vis spectroscopic responses were further studied under physiological and analytical conditions (varying the ionic strength and in real sample matrices) to validate the stability of the probe.

2.3. Evaluation under physiological and analytical conditions

2.3.1. Selectivity studies. Competitive binding studies were performed to evaluate the interference of other amino acids in arginine detection. To accomplish this, colorimetric and spectral changes of probe **P1**–arginine (100 μM : 50 μM) were recorded in the presence of 50 μM other amino acids. The selectivity of **P1** towards arginine was further evaluated by its consistent performance upon varying the ionic strength and in real biological matrices, confirming its robustness under practical conditions.

2.3.2. Effect of ionic strength and biological media. To examine the robustness of probe **P1** under physiological conditions, its sensing performance was evaluated upon varying the ionic strength and in the presence of complex biological matrices. Different concentrations of NaCl (0 to 100 mM) were added to arginine solutions to mimic physiological ionic environments, and the probe response was monitored. Additionally, the performance of the sensor was checked in complex biological media using bovine serum albumin (BSA, 1 mg mL^{-1}) to mimic a serum-like matrix. The detection response was recorded *via* absorption measurements to confirm the stability, selectivity, and sensitivity of **P1** under biological conditions. Based on the stable response under physiological conditions, binding stoichiometry and limit of detection studies were performed.

2.4. Binding stoichiometry analysis and the limit of detection

For the binding stoichiometry analysis, stock solutions of probe **P1** (1 mM in DMSO) and arginine (1 mM in double-distilled water) were prepared. A series of mixtures were prepared by varying the volumes of probe **P1** (0.3 to 3 mL) and arginine (3 to 0.3 mL), while keeping the total volume in the cuvette constant at 3 mL. The absorption spectra were recorded at 440 nm of the probe (X_{probe}) against $(A_0 - A) \times X_{probe}$, where A_0 and A represent the absorbance values.

The limit of detection (LOD) for arginine detection using the probe was determined using the equation:

$$\mathrm{LOD} = \frac{3\sigma}{S},$$

where σ is the standard deviation of the blank measurements, and S is the slope of the calibration curve. The standard

deviation of the calibration curve was determined using four replicate absorbance measurements.

The interaction strength between arginine and the probe **P1** was assessed with an absorption titration experiment. Arginine (0 to 100 μM) was gradually added in 10 μL increments. The resulting absorption spectra were recorded and utilized to generate a Benesi–Hildebrand (B–H) plot of $1/(A - A_0)$ *versus* 1/[Arginine], enabling the evaluation of the binding interaction. The binding constants were determined using the slope of the B–H plot from the equation.

$$\frac{1}{A - A_0} = \frac{1}{K_b(A_{max} - A_0)C} + \frac{1}{A_{max} - A_0}.$$

Here, A_0 and A represent the absorbance of the probe in the absence and presence of arginine, respectively. A_{max} refers to the highest absorbance recorded following the addition of arginine. K_b is the binding constant, and C denotes the concentration of arginine. To gain mechanistic insights into the selective detection of arginine during the amino acid sensing experiment, DFT calculations were performed.

2.5. DFT studies

In the present work, all calculations were performed using Gaussian 09 software.[24] The selected probe (**P1**), arginine analyte (assumed as **A1**), and the resulting product (assumed as **C1**) were optimized using the hybrid-exchange correlation functional CAM-B3LYP (Coulomb-attenuated mixing Becke three-parameter Lee–Yang–Parr)[24] along with a split-valence double-zeta basis set, 6-31+G(d,p). The selection of CAM-B3LYP/6-31+G(d,p) was based on the effectiveness of this level of theory in studying organic molecules involved in charge-transfer or long-range intermolecular interactions. To incorporate the solvent effect, the analysis was carried out using a gas phase, cyclohexane, water, and DMSO in CPCM (conductor-like polarizable continuum model) at the same level of theory.[24] Based on the theoretical outcome, DMSO was selected for further studies, which also aligns with the experimental solvent system used to conduct the current work (Table S1). The absence of negative frequencies in the vibrational spectra of **P1**, **A1**, and **C1** confirms the formation of stable, energy-minimized geometries. The PES scanning plot was generated to understand the interactions formed within complex **C1** (**P1**···**A1**). This scanning plot maps the energy variation along the reaction coordinates and identifies the product and any intermediate states formed. NBO calculations were performed to analyze the charge change in **P1** during complex formation. Moreover, to understand the hydrogen bonds and other non-covalent interactions formed within **C1**, RDG and NCI plots were generated using the Multiwfn program.[24] These plots were created using visual molecular dynamics (VMD) software.[25] In addition to its selectivity sensing ability, the therapeutic potential of compound **P1** was further explored through combined *in silico* and biological assays evaluating its anticancer efficacy.

2.6. Molecular docking studies

2.6.1. PASS online. Based on the target prediction outcome extracted from the freely available web resource, PASS online tool, Mcl-1 was observed as the potential therapeutic target having a probable activity (P_a) of 0.898 and a probable inactivity (P_i) of 0.003 (**https://www.way2drug.com/passonline**). The Mcl-1 enzyme is known to cause tumorigenesis and resistance to anticancer therapies; thus, it is considered an attractive anticancer target.[26] Thereafter, the Mcl-1 enzyme with PDB ID 5FC4 was selected to perform molecular docking and interaction analysis to study the binding of the selected compound **P1** with the enzyme.

2.6.2. Molecular docking analysis. To study the interaction pattern of the selected compound **P1** with the Mcl-1 enzyme, molecular docking studies were conducted using the FlexX module[27] of the SeeSAR v13.1.1 software.[28] The FlexX module implements the modified Bohm scoring function to calculate the binding affinity between the compound and macromolecule.[29] To validate the docking protocol, we first performed redocking studies using known Mcl-1 inhibitors, 5WL, 5X2, 5X3, 70R, LC3, and Q0D corresponding to PDB IDs 5FC4, 5FDO, 5FDR, 5LOF, 5WIX, and 6U63, respectively. Based on the resolutions, 5FC4 was selected for docking calculations with the selected molecule **P1**. During docking calculations, the Protein Editor Mode of the software was used to prepare the protein chain. While performing protein preparation, missing side chains and hydrogen atoms were added automatically, bond orders were assigned, alternate amino acids and water molecules were removed, and hydrogen bond networks were optimized, along with the generation of hetero protonation states at pH 7.4. Thereafter, the Binding Site Mode of the software was utilized to generate the binding pocket based on the co-crystallized ligand of the macromolecule. The top ten poses were generated from the docking calculation. The 2D interaction plot of the docked protein–ligand complex was constructed using the Discovery Studio visualizer.

2.7. Cell viability (MTT assay)

2.7.1. Cell culture. To complement the molecular docking studies, *in vitro* cytotoxicity of **P1** was evaluated using the MTT assay on cancer cells MCF7 (breast cancer cells) and HeLa (cervical cancer cells). The safety evaluation of **P1** on normal cells was assessed through the MTT assay on WS1 (normal fibroblast cells). The MCF7, HeLa and WS1 cells were procured from the National Center for Cell Science (NCCS), Pune, and cultured in Dulbecco's modified Eagle medium (DMEM) for MCF7 and HeLa and in Eagle's minimum essential medium (EMEM) for WS1 supplemented with 10% fetal bovine serum (FBS) (Gibco), 1–2% non-essential amino acids and 1% antimycotic-antibiotic solution (HiMedia). The cells were maintained at 37 °C in a 5% CO_2 incubator. Sub-culturing was carried out using a 0.25% Trypsin Phosphate Versene Glucose (TPVG) solution (HiMedia), until the cells reached approximately 80% confluency.

The IC_{50} values of the compound were determined using the MTT assay. The cells (10^4 cells per well) were seeded in a 96-well plate containing 10% DMEM. Serial dilutions of the compounds (ranging from 5 μM to 100 μM) were prepared in incomplete media, and treatments were applied once the cells reached approximately 70% confluency. After 24 hours of incubation, 3-(4,5-dimethylthiazol-2-yl)-2,5-diphenyltetrazolium bromide (MTT; 5 mg mL^{-1}) was added and incubated for 4 hours. Post incubation, the MTT solution was removed, and 150 μL of DMSO was added to each well to dissolve the resulting formazan crystals. Absorbance was then recorded at 540 nm using a Synergy HTX multimode reader.[30]

2.7.2. Apoptosis assay by Annexin V–propidium iodide (PI) binding. Flow cytometry analysis through Annexin V–PI (Becton Dickinson) binding on the cells was performed to reveal the percentage of cells that are viable and undergoing apoptosis, and necrotic cells upon **P1** treatment. 100μL of the treated cell suspension ($\sim 1 \times 10^6$ cells per mL) in binding buffer (1×) was incubated in the dark with Annexin V-FITC and PI for 15 minutes at room temperature. Then, the percentage of viable/apoptotic/necrotic cells was evaluated using a flow cytometer (FACS-Becton Dickinson).[31]

2.7.3. Haemolysis assay. To evaluate the biocompatibility of compound **P1**, a haemolysis assay was performed using human red blood cells. Whole blood was collected from a healthy individual in EDTA-coated vacutainer tubes. The collected blood samples were treated with varying concentrations of the compounds. Negative control was a sample treated with 1× PBS (0% haemolysis), and positive control was a sample treated with 3% hydrogen peroxide (100% haemolysis). After incubation for 3 hours, the tubes containing blood samples were centrifuged at 1500 rpm for 10 min to collect the plasma. The OD was measured at 540 nm and 655 nm,[23,32] and the percentage of haemolysis was calculated using the following formula:

$$\%\ \text{Haemolysis} = 100 \times \frac{\text{Sample absorbance}_{540-655\text{nm}} - \text{Negative control absorbance}_{540-655\text{nm}}}{\text{Positive control absorbance}_{540-655\text{nm}} - \text{Negative control absorbance}_{540-655\text{nm}}}.$$

Following the haemolysis assay, molecular dynamics simulations were conducted to study the stability of the **P1**–Mcl-1 complex at the molecular level.

2.8. Molecular dynamics simulations

Molecular dynamics simulations were conducted on 5FC4 complexed with the reference (5WL) and the docked molecule (**P1**) for 300 ns using the AMBER99SB force field of GROMACS 2022.4.[33,34] The topologies of both molecules, *i.e.*, 5WL and **P1**, were generated using ACPYPE.[35] Each system was placed in a dodecahedron simulation box with a minimum distance of 1 nm between the protein surface and the box edge in all directions. The SPC216 water model was used for solvation, and the systems were neutralized by adding Na^+ and Cl^- ions. Energy minimization was performed using the steepest descent algorithm for 50 000 steps to eliminate steric clashes and unfavourable contacts, with the maximum force constrained below 1000 kJ mol^{-1} nm^{-1}. Following minimization, position-restrained equilibration was carried out in two stages: first under the NVT ensemble (constant number of particles, volume, and temperature) for 100 ps using the Berendsen thermostat[36] to maintain the temperature at 300 K; then under the NPT ensemble (constant number of particles, pressure, and temperature) for 100 ps using the Parrinello–Rahman barostat to maintain pressure at 1 bar.[37] Long-range electrostatic and van der Waals interactions were computed using the Particle-Mesh Ewald (PME) method with a cutoff of 1 nm.[38] Bond constraints were applied using the LINCS algorithm to maintain fixed bond lengths.[39] Production molecular dynamics simulations were then carried out using default GROMACS parameters, with system coordinates recorded every 2 fs. Various structural and dynamic properties were analyzed, including root mean square deviation (RMSD), root mean square fluctuations (RMSF), radius of gyration (RoG), and hydrogen bonding (H-bonds), and plotted using GRACE.[40] Moreover, Coulombic interaction energy and Lennard-Jones energy both were calculated.

3. Results and discussion

3.1. Structural characterization

The ^{1}H NMR spectrum of the synthesized compound **P1**, recorded in DMSO-d_6, displays a characteristic singlet at $\delta \sim 12.10$ ppm, which can be attributed to the –NH proton of the hydrazone moiety (–C═N–NH–). This downfield shift is consistent with strong intramolecular hydrogen bonding interactions and the deshielding effect of the adjacent imine and aromatic groups.[41] Additionally, the imine proton (–CH═N–) appears as a singlet in the region of δ 9.967 ppm, confirming the successful formation of the hydrazone linkage. The presence of these two distinct signals confirms the proposed structure. The IR spectrum shows a strong band at 1620 cm^{-1} for C═N stretching of the hydrazone and a peak at 1510 cm^{-1} attributed to the asymmetric stretching of the nitro group, confirming the presence of both imine and $–NO_2$ functionalities (Fig. S2).

3.2. Colorimetric detection of arginine

The colorimetric response of probe **P1** toward the selected amino acids and ornithine was evaluated by adding them to its solution. Among them, only arginine induced an immediate visible color change from yellow to red, while the addition of other amino acids resulted in no noticeable color change (Fig. 1). The initial colorimetric response of **P1** upon arginine addition was further validated and quantified *via* UV-Vis

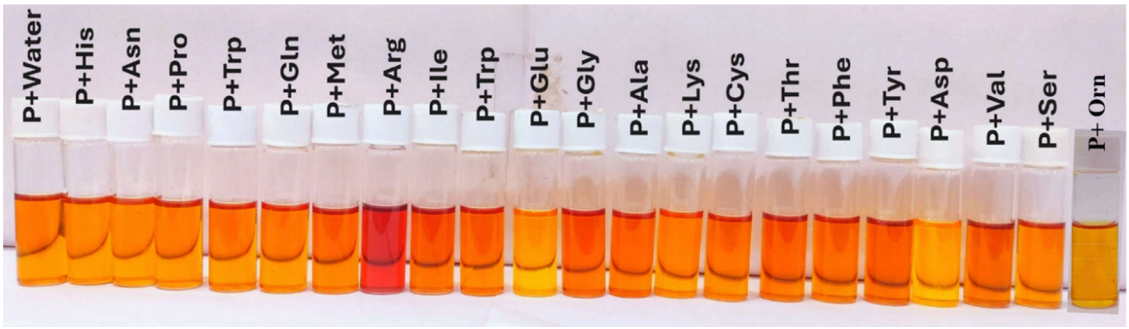

Fig. 1 Naked eye colour change of probe **P1** (100 μM) in the presence of different amino acids.

absorption studies, providing structural evidence of the binding interaction.

3.3. UV-Vis absorption studies and spectral analysis

The UV-Vis absorption spectrum of probe **P1** (100 μM) recorded in DMSO exhibited a broad band ranging between 300 and 500 nm, with distinct absorption maxima at 369 nm and 440 nm (Fig. 2A), likely corresponding to n–π* or π–π* transitions within the probe's highly conjugated system. As shown in Fig. 2B, the charge transfer band centered at 440 nm decreased in intensity and underwent a red shift from 20 nm to 460 nm. Additionally, a new absorption band emerged at 540 nm with a clear isosbestic point at 463 nm, indicating the formation of a stable complex between **P1** and arginine. Upon addition of various amino acids (100 μM), including alanine, asparagine, aspartic acid, cysteine, glutamic acid, glutamine, glycine, histidine, isoleucine, leucine, lysine, methionine, phenylalanine, serine, proline, tyrosine, tryptophane, threonine, valine, and

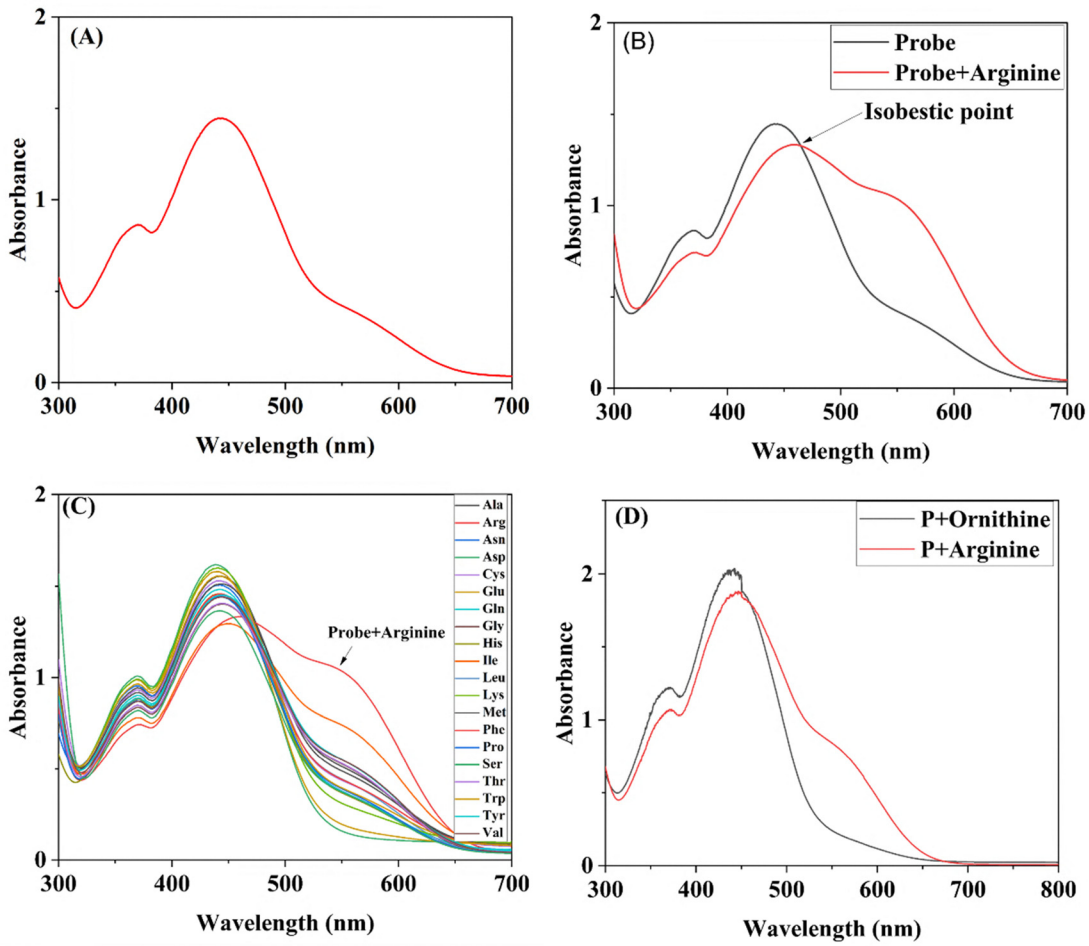

Fig. 2 (A) UV absorbance of probe **P1** (100 μM) in 90% DMSO:Water. (B) Absorption spectra of probe **P1** and **P1** + arginine. (C) UV-Vis spectral changes in probe **P1** on the addition of 100 μM of different amino acids. (D) UV-Vis spectral change in probe **P1** on addition of 100 μM ornithine (structural homolog).

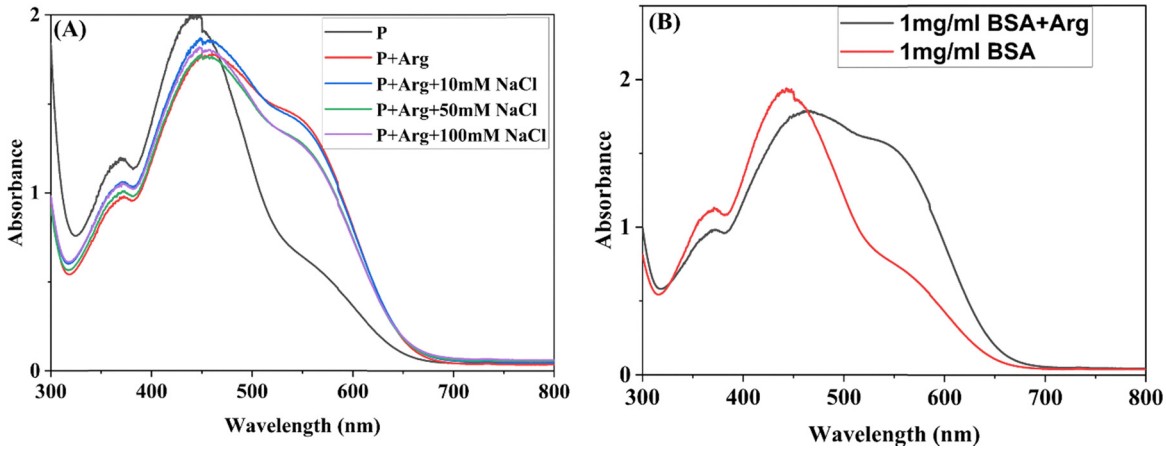

Fig. 3 (A) UV-Vis absorption spectra of **P1** (100 μM in the presence of different concentrations of salt (NaCl, 10 to 100 mM)). (B) The UV-Vis absorption spectra of probe **P1** and **P1** + arginine in the presence of bovine serum albumin (BSA, 1 mg mL^{-1}) [red and black lines, respectively].

ornithine, no significant changes were observed in the absorption spectra, except for a slight alteration with isoleucine. In contrast, the addition of arginine led to a marked change in the absorption profile, accompanied by a visible color change (Fig. 2C). Therefore, no significant change in the absorption spectra for these amino acids and structural homologs (Fig. 2D) confirms the sensor's selectivity toward arginine detection. To ensure the practical applicability of the UV-Vis response, spectral analyses were further extended under physiological and analytical conditions to check the stability of the probe and efficiency in sensing in a biological environment.

3.4. Evaluation under physiological and analytical conditions

3.4.1. Effect of ionic strength (NaCl) and biological media. To simulate the effect of pH and ionic strength on the probe's sensing behaviour, different concentrations of NaCl were added to mimic the ionic content typically found in biological fluids. The UV-Vis absorption spectra of the probe–arginine complex were recorded in the presence of increasing salt concentrations (10 mM to 100 mM). The absorption spectra show a minimal decrease in intensity with an increase in the salt concentration; however, the characteristic peak at 540 nm corresponding to arginine binding remains clearly distinguishable even at 100 mM salt [Fig. 3A]. This indicates that the probe retains its sensing capability and structural integrity in high-ionic-strength environments. The probe performs best at sensing at neutral pH, according to pH-dependent studies. Maintaining physiological pH conditions is crucial for accurate detection, as evidenced by the reduced or non-specific responses that occurred from significant deviation from this pH. Together, these results demonstrate that the probe is stable and selective in biologically realistic settings.

To evaluate the sensor's performance in a biologically relevant matrix, a 1 mg mL^{-1} solution of bovine serum albumin (BSA) was prepared and used as a model protein. A mixture of 300 μL of BSA solution and 300 μL of the probe solution was prepared, and the volume was adjusted to 3 mL using DMSO. In another setup, 300 μL each of the BSA solution, arginine solution, and probe solution were combined and similarly diluted to a final volume of 3 mL, and the corresponding absorption spectra were recorded. The absorption spectra revealed that the presence of BSA had no noticeable interference with the sensor's response, indicating that the probe retains its selectivity and performance even in a protein-rich environment (Fig. 3B).

Following the confirmation of probe stability in various ionic strengths and biological media, a time-based study was conducted to evaluate the rapidity and consistency of the arginine-detection response.

3.4.2. Time-based study. To evaluate the time-dependent response of the probe towards arginine, a time-based UV-Vis spectroscopic study was performed. The absorbance of probe **P1** at 540 nm changed promptly upon adding 1 equivalent of arginine and remained consistent afterward (Fig. 4). Thus, the

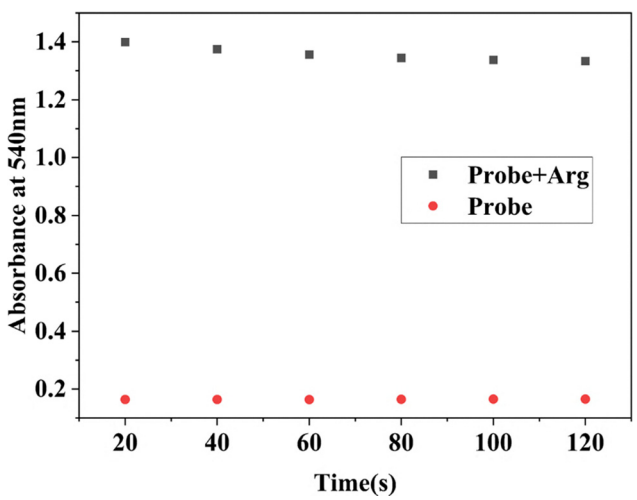

Fig. 4 Time-dependent absorbance at 540 nm of 100 μM probe **P1** with 1 equiv. arginine.

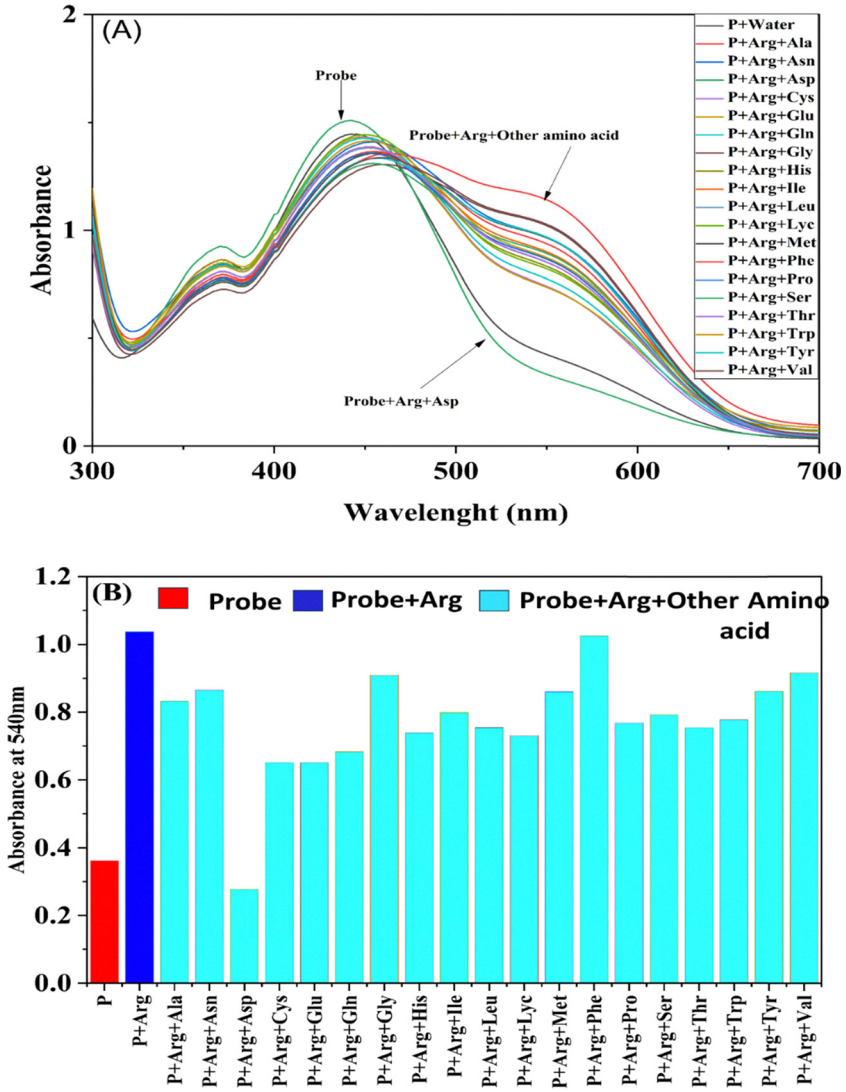

Fig. 5 (A) UV-Vis absorption spectral changes of probe **P1** in 90% DMSO:water upon the addition of various amino acids (50 μM) in the presence of arginine (50 μM). (B) The corresponding absorbance values of probe **P1** for different amino acids, measured at 540 nm.

probe is ideal for real-time arginine detection due to its rapid sensing ability. On observing the rapid sensing ability of **P1** through time-based studies, selectivity experiments were conducted to check the specificity towards arginine sensing.

3.4.3. Selectivity studies. Selectivity studies were performed with the aim of evaluating the specificity of probe **P1** towards arginine in comparison to other structurally similar amino acids. An interference experiment was performed to assess the selectivity of probe **P1** for arginine in the presence of competing amino acids in a complex matrix, as illustrated in Fig. 5. The absorption spectra of **P1** in the presence of arginine (50 μM) exhibited a consistent pattern even in the presence of other amino acids (50 μM), as shown in Fig. 5A. However, slight interference was detected in the presence of aspartic acid, indicating partial interaction. This interaction could be attributed to its acidic nature, which may cause a minor spectral change by weak electrostatic interactions in the sensing environment, leading to a mild UV response without a significant colour change. Despite this, the chemosensor probe **P1** demonstrated high selectivity for arginine over other amino acids under identical conditions (Fig. 5B). This selectivity is attributed to the preferential interaction between **P1** and arginine, likely driven by hydrogen bonding and electrostatic interactions. These findings highlight the potential of probe **P1** as a reliable sensing platform for arginine detection in biological and environmental applications. Following the confirmation of the selectivity of **P1** towards arginine under controlled conditions, its practical applicability was further evaluated through real sample analysis using commercially available dietary supplements.

3.4.4. Real sample analysis (arginine sensing in dietary supplements). To test the practical applicability of the synthesized sensor under practical conditions for arginine detection, a commercially available arginine supplement powder was used as a real sample. A total of 115 mg of the supplement powder was dissolved in 5 mL of distilled water, followed by filtration to

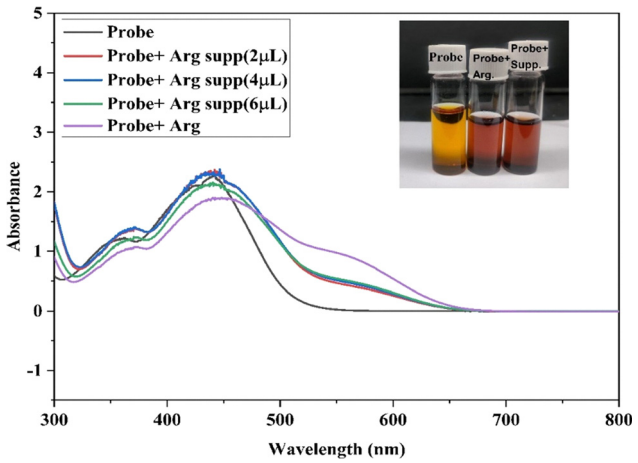

Fig. 6 Colorimetric sensing test of arginine by probe **P1** using a real arginine supplement.

remove any insoluble impurities. The resulting clear solution was used for further analysis. Sequential aliquots (2 μL, 4 μL, and 6 μL) of the prepared sample were added to a 100 μM solution of **P1** in DMSO, and the corresponding absorption spectra were recorded. Additionally, a mixture containing 100 μM of standard arginine and the prepared supplement sample was also analysed to assess the sensor's performance in complex matrices. The absorption spectra of **P1** containing real arginine samples show a change in the colour visible to the naked eye, and the same absorption pattern in the UV spectra (Fig. 6) indicates its potential for use in real-life applications.

3.5. Binding stoichiometry analysis and limit of detection

To gain a deeper understanding of the interaction between Probe **P1** and arginine, UV-Vis titration experiments were conducted. Upon the stepwise addition of arginine (0–30 μM) to the **P1** solution, a gradual decrease in absorbance at 440 nm was observed, accompanied by a slight red shift to 460 nm and the emergence of a new absorption peak at 540 nm, as illustrated in Fig. 7A. The detection limit of **P1** was found to be 1.24 nM. This implied that probe **P1** could be used for arginine detection at very low concentrations. The analytical performance of probe **P1**, having a detection limit of 1.24 nM (Fig. 7A), was compared with that of several reported arginine-responsive probes, highlighting its superior sensitivity (Table S2). To further elucidate the binding interaction, both the binding constant and stoichiometry were evaluated using a Benesi–Hildebrand (B–H) and Job's plot, respectively. The B–H plot of $1/(A - A_0)$ *versus* 1/[Arginine] displayed good linearity (R^2 = 0.9912), confirming a 1 : 1 binding stoichiometry between **P1** and arginine (Fig. 7B). The binding association constant (K_a) was calculated to be $3.74 \times 10^4\ M^{-1}$. Additionally, the Job's plot exhibited a clear maximum at a 0.5 molar ratio (Fig. 7C), further supporting a 1 : 1 stoichiometric interaction between **P1** and

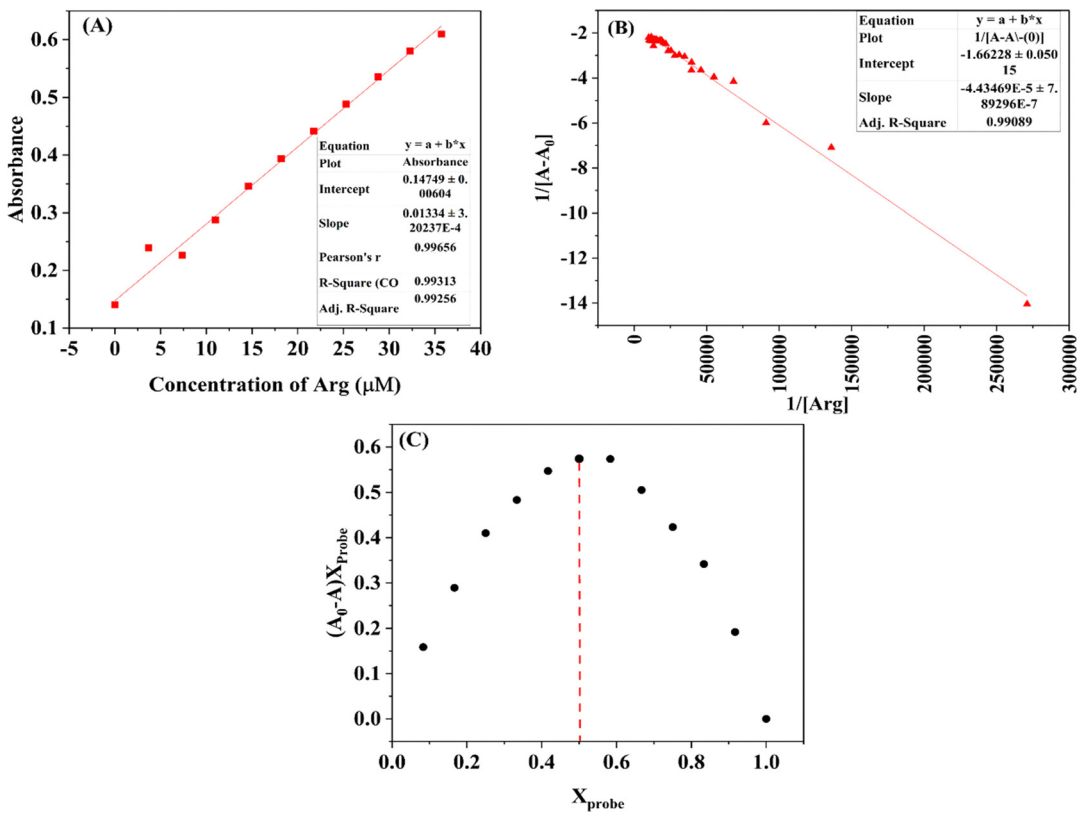

Fig. 7 (A) The absorption spectrum of probe **P1** (100 μM) on the consecutive addition of arginine (0–30μM); (B) the Benesi–Hildebrand plot for **P1**–arginine interaction; (C) Job's plot confirming the binding stoichiometry between probe **P1** and arginine, where X_{probe} denotes the mole fraction of **P1**.

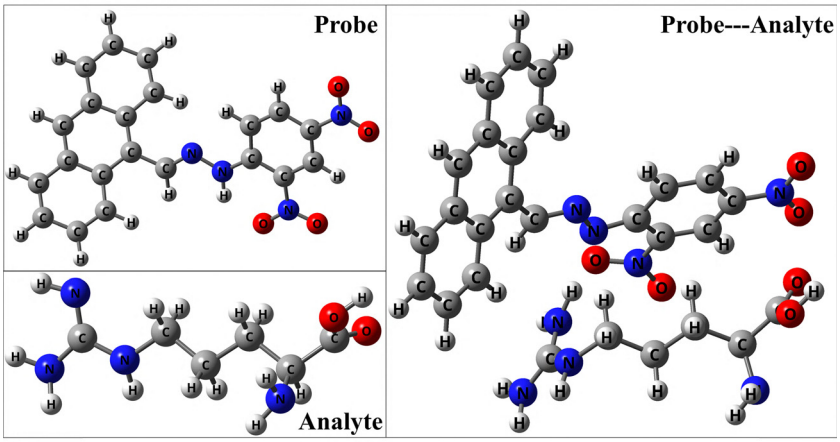

Fig. 8 Molecular geometries of the optimized probe (**P1**), analyte (**A1**), and the product (**P1**···**A1**) with atomic labelling of all atoms obtained at the CAM-B3LYP/6-31+G(d,p) level of theory using the CPCM-DMSO solvation model.

arginine. The insights gained from binding stoichiometry analysis and limit of detection studies confirm the selective interaction of **P1** and arginine. Based on this, a proposed sensing mechanism was further outlined to explain the interaction between **P1** and arginine.

3.6. Proposed sensing mechanism

To gain further insight into the interaction between probe **P1** and arginine, NMR titration experiments were performed, and the addition of 1 equivalent of arginine to **P1** in DMSO-d_6 resulted in the complete disappearance of the signal at 12.10 ppm (Fig. S4). Additionally, signals at 9.97, 8.90, 8.43, and 8.06 ppm exhibited noticeable broadening, suggesting changes in the chemical environment due to **P1**–arginine interactions. These spectral changes indicate that the binding likely involves the N–H proton of the Schiff base scaffold. The proposed binding mechanism is depicted in Fig. S4. Furthermore, the interaction mode is corroborated by theoretical investigations using DFT calculations.

3.7. DFT studies

To gain deeper insight into the sensing of arginine by probe **P1** at the molecular level, DFT calculations were conducted.

3.7.1. Ground state geometry optimization. The ground state optimized geometries of **P1**, **A1**, and **C1** are shown in Fig. 8. These geometries correspond to the minimum energy points, as indicated by the absence of negative frequency in the frequency calculations (Tables S3–S5). These optimized geometries were employed for further calculations.

3.7.2. UV-Vis absorption spectra and molecular orbital analysis. Experimental studies reveal spectral variations in **P1** upon the addition of **A1**, with the 440 nm absorption band decreasing and a new peak emerging at 540 nm, as shown in Fig. 9. The theoretical studies conducted on **P1** and **C1** also follow the same trend (Fig. 9).

As observed in Table 1, the highest oscillatory strength is observed for the $S_0 \rightarrow S_1$ transition for **P1** and the $S_0 \rightarrow S_2$ transition for **C1**, which depicts the allowed transition. For the obtained transitions, the respective oscillator strength, orbital contribution, and % contribution of **P1** and **C1** are tabulated in Table 1. For **P1**, the $S_0 \rightarrow S_1$ transition was observed at 416.80 nm (2.97 eV) with a maximum oscillatory strength of 0.68, whereas in the case of **C1**, the $S_0 \rightarrow S_2$ transition was observed at 427.44 nm (2.97 eV) with a maximum oscillatory strength of 0.95. The theoretical wavelengths were in good agreement with the experimental outcome, as in both cases, upon binding, a red shift is obtained in the spectra of **C1**. Moreover, the increase in the oscillatory strength depicts the highly intense absorption, which is considered ideal for sensing. Therefore, considering the situation, it can be predicted that binding of **A1** with **P1** increases the charge transfer interactions. FMO analysis also reveals the major contribution in the transitions of **P1**, which was observed due to HOMO to LUMO (39.78%), HOMO to LUMO+1 (28.42%), HOMO to

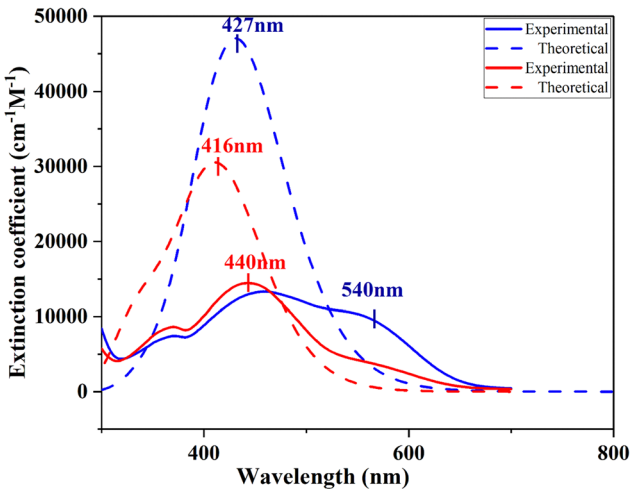

Fig. 9 Graphical representation of the experimental UV-Vis spectra of the probe and product (straight lines), and the calculated absorption band (dotted lines) generated at the CAM-B3LYP/6-31+G(d,p) level of theory using the CPCM-DMSO solvation model. Red color corresponds to the probe, and the blue color corresponds to the product.

Table 1 Calculated wavelengths (nm) along with the experimental values (nm), their corresponding oscillatory strengths, and % contribution of the transition of probe **P1** and product **C1**, calculated at the B3LYP/6-31+G(d,p) level of theory using the CPCM-DMSO model

Molecules	Probe (P1)	Product (**P1**···**A1**)
Calculated transition wavelength (nm)	416.8	427.44
Calculated energy (eV)	2.97	2.9
Experimental values (nm)	440	540
Electronic transition[a]	$S_0 \rightarrow S_1$	$S_0 \rightarrow S_2$
Oscillatory strength (*f*)	0.68	0.95
Main contribution	H−1 → L	H−1 → L
	H → L	H−1 → L+2
	H → L+1	H → L
	H → L+2	H → L+1
Configuration interaction (CI)	−0.21	−0.18
	0.45	0.14
	0.38	0.44
	−0.29	0.47
Contribution of transition[b] (%)	8.98	6.55
	39.78	4.03
	28.42	38.89
	17.05	44.74

[a] Selected low-lying excited state. [b] = 2 × $(CI)^2$ × 100.

LUMO+2 (17.05%), and HOMO–1 to LUMO (8.98%). Similarly, in **C1**, the major contribution was observed because of HOMO to LUMO+1 (44.74%), HOMO to LUMO (38.89%), HOMO–1 to LUMO (6.55%), and HOMO–1 to LUMO+2 (4.03%), suggesting the formation of new electronic interactions in **C1** (Fig. 10). Moreover, as depicted in the PES and NCI calculations, the observed bathochromic shift also supports the proton transfer. The HOMO–LUMO energy analysis reveals a slight reduction in the energy gap from 0.059 eV (**P1**) to 0.0506 eV (**C1**), indicating increased electronic delocalization. Moreover, the major orbital transitions (HOMO to LUMO) suggest a potential intramolecular charge transfer (ICT) mechanism. The orbital orientation across the donor and acceptor regions in Fig. 10 also supports the interpretation. The same was studied *via* PES plots.

3.7.3. Natural bond orbital analysis. The binding of the analyte to the probe (**P1**) was evaluated through NBO charge calculations. The calculated natural charges on key atoms are presented in Fig. 11. The results provide clear evidence of charge redistribution upon interaction with **A1**, highlighting a proton transfer event that contributes to the stabilization in **C1**. Notably, atom N63 shows a significant gain in electron density (Δq = +0.147), consistent with proton uptake, while atom N25 becomes more negative (Δq = –0.201), indicating its role as the proton donor. A slight decrease in the negative charge on atom N24 (Δq = +0.057) suggests electron delocalization or reduced participation in hydrogen bonding following the transfer. Meanwhile, atom C26 exhibits an increase in positive charge (Δq = +0.175), likely due to the overall electronic rearrangement in the system rather than direct involvement in bond formation. These charge shifts support a mechanism involving

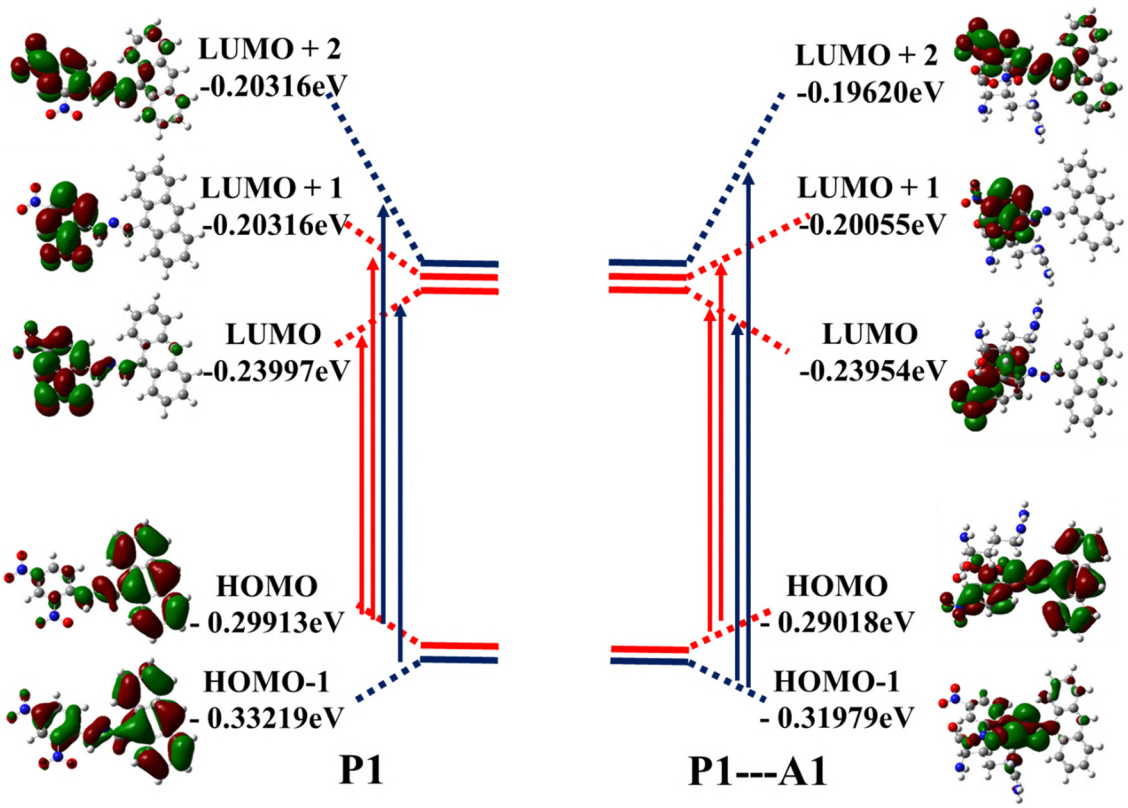

Fig. 10 Frontier molecular orbital of ground state geometry of probe **P1** and complex (**P1**···**A1**), generated at the CAM-B3LYP/6-31+G(d,p) level of theory using the CPCM-DMSO solvation model. Red color transitions represent the major contribution.

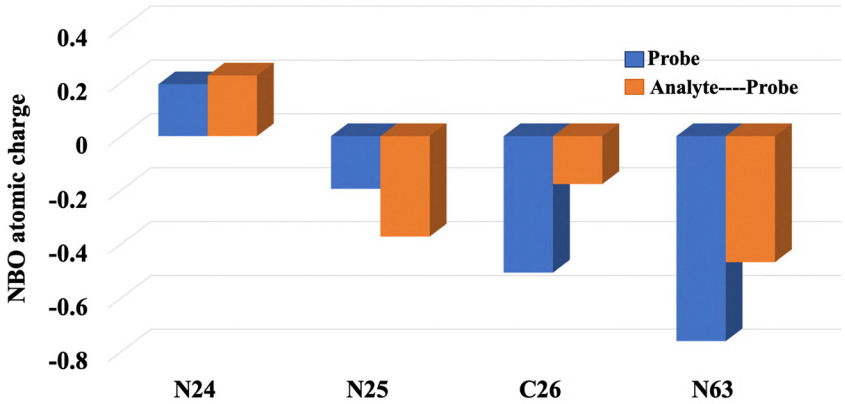

Fig. 11 Visual representation of atomic natural charges obtained from NBO analysis generated using the CAM-B3LYP/6-31+G(d,p) level of theory and the CPCM-DMSO solvation model.

proton transfer from N25 to N63, accompanied by electronic reorganization that stabilizes the resulting product. This interpretation is further supported by PES analysis, which confirms the formation of a more stable, low-energy product configuration, in agreement with the experimental observations.

3.7.4. Noncovalent interaction index. The reduced density gradient (RDG) method is a powerful tool for identifying and analyzing non-covalent interactions. RDG scatter plots, along with non-covalent interaction (NCI) plots, provide a visual representation of these interactions between molecular entities. In this technique, the RDG is plotted against the electron density multiplied by the sign of the second eigenvalue of the Hessian matrix ($\mathrm{sign}(\lambda_2)\rho$).[42] As shown in Fig. 12, this approach effectively captures both intermolecular and intramolecular interactions. Green spikes on the positive side of the $\mathrm{sign}(\lambda_2)\rho$ axis indicate van der Waals interactions, while red spikes correspond to steric repulsions. The NCI analysis of the probe structure reveals a prominent hydrogen bond interaction, indicated by a distinct blue region at negative values of $\mathrm{sign}(\lambda_2)\rho$ in the scatter plot, highlighting the highly directional nature of the interaction. This corresponds to the proton being closely associated with the donor nitrogen atom of the imine group, while simultaneously engaging with the acceptor oxygen atoms of the nitro group. Upon introduction of **A1**, a

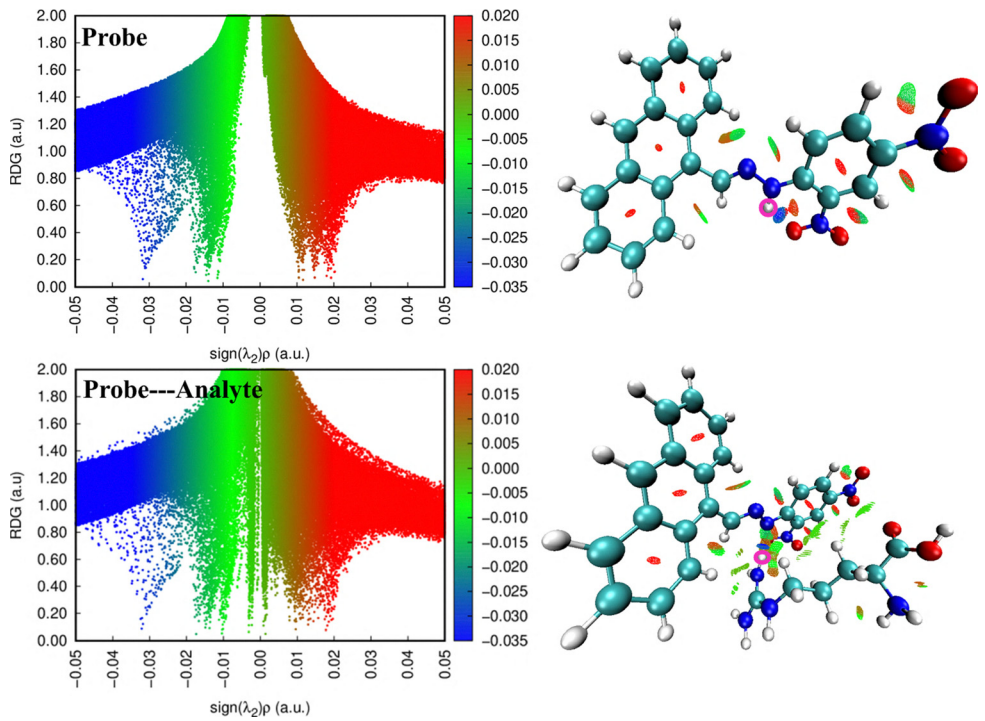

Fig. 12 NCI isosurfaces and RDG scatter plots for probe **P1** and product (**P1**···**A1**) generated at the CAM-B3LYP/6-31+G(d,p) level of theory using the CPCM-DMSO solvation model. The RDG cut-off is $\mathrm{sign}(\lambda_2)\rho$ = 0.5 a.u., with a color scale from −0.030 to 0.020 a.u., where blue, green, and red indicate attractive, van der Waals, and repulsive interactions, respectively.

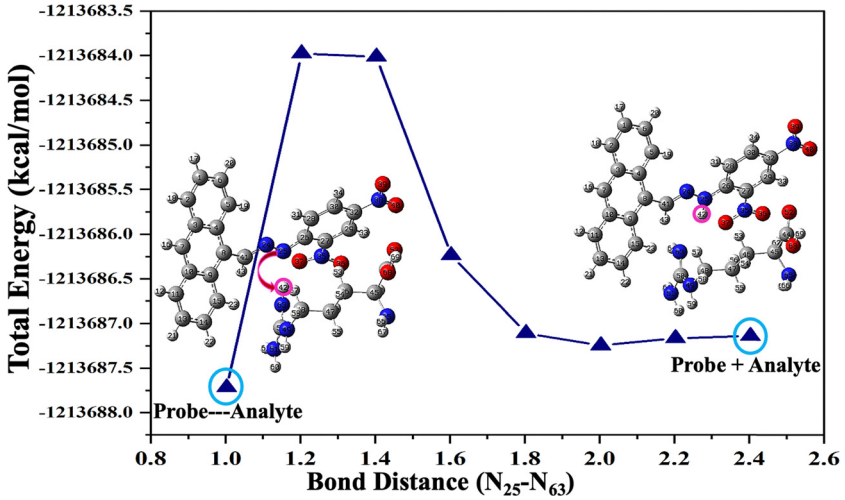

Fig. 13 Potential energy scanning plot generated between probe **P1** and analyte **A1** with a bond length of N25–N63, calculated at the CAM-B3LYP/6-31+G(d,p) level of theory using the CPCM-DMSO solvation model. The pink color represents the atoms involved in the proton shift.

notable attenuation and shift of this interaction are observed, evidenced by a reduction in the intensity of the blue region and the emergence of broader green areas in the NCI plot of the product. This transition reflects a weakening of the hydrogen bond and an increase in van der Waals interactions, consistent with a proton transfer event that stabilizes the product through a reorganization of the surrounding noncovalent interaction network.

3.7.5. Potential energy scanning analysis. To understand the mechanistic insights for a sensor, a potential energy surface (PES) scan was generated with a focus on key bond length changes between atom N25 and N64, as shown in Fig. 13. A significant shortening of the N63–H42 bond from 2.400 Å to 1.00 Å was observed in **C1**, indicating strong bond formation. Concurrently, the N25–H42 bond elongates from 1.028 Å to 1.97 Å, suggesting proton transfer during the process (Table S6). These two changes point to a bond substitution or migration event as the central feature of the reaction. Other bonds show minimal variations, indicating localized changes around the reactive centre. This analysis highlights a concerted mechanism involving bond breaking and formation, with the formation of the N63–H42 bond being the driving force behind the observed structural shift. The formation of the bond was further verified by the NCI calculations.

3.7.6. Electrostatic potential analysis. The ESP plots used a color code to predict the nature of the molecular region. The red region depicts the high electron density area, the blue region represents the low electron density area, and the green/yellow region represents the neutral part of the molecule. The ESP plots of **P1** and **C1** are shown in Fig. 14. It is visible that the hydrogen atom involved in the shifting belongs to the blue area; thus, the part can act as a hydrogen bond donor. Moreover, the ESP plot of **C1** is more polarized, suggesting the formation of noncovalent interactions, and the same has been explained in NCI calculations. Thus, combined PES, NCI, UV-Vis, and ESP calculations confirm the proton transfer during the sensing of **A1**, which is facilitated by intramolecular charge transfer (ICT), as depicted by FMO analysis. This acts as the primary mechanism responsible for showing the optical response of probe **P1** in the presence of the analyte arginine.

Apart from its sensing capability, the potential of **P1** was further evaluated *via* combined *in silico* and biological studies to check the anticancer activity of the probe.

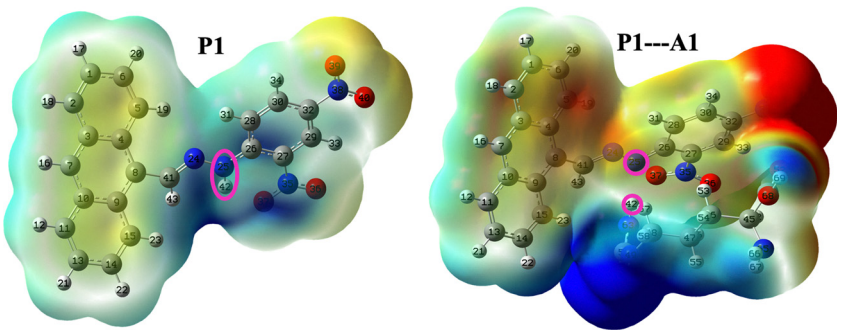

Fig. 14 Electrostatic potential plots of probe **P1** and complex (**P1**···**A1**), generated at the CAM-B3LYP/6-31+G(d,p) level of theory using the CPCM-DMSO solvation model. The pink color represents the atoms involved in the proton shift.

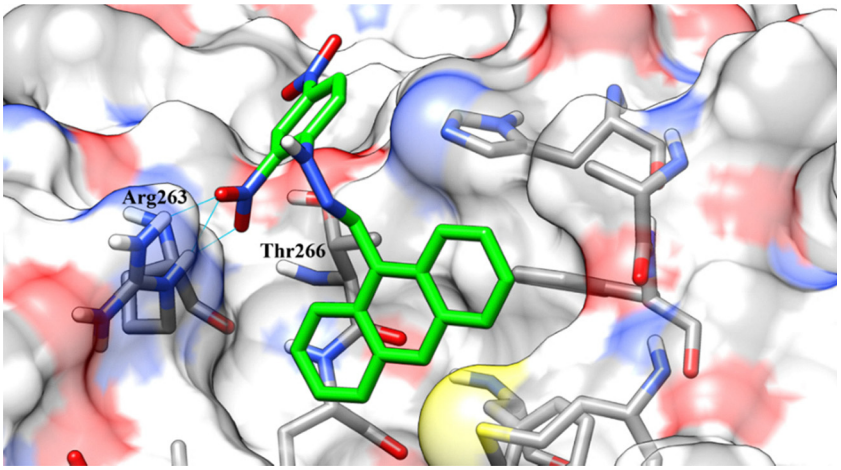

Fig. 15 3D docked complex of molecule **P1** within the active site of the Mcl-1 protein with PDB ID 5FC4.

3.8. Molecular docking analysis

On performing molecular docking of the selected compound **P1** with the Mcl-1 protein, it was observed that **P1** binds well within the active site of the Mcl-1 protein, as shown in Fig. 15. Also, on comparing our compound **P1** with the selected reference inhibitors, 5WL, 5X2, LC3, Q0D, 5X3, and 70R, it was observed that all molecules bind in the same binding pocket of the enzyme (Fig. S5). On comparing the docking score, it was observed that **P1** displayed the highest docking score of -15.48 kcal mol^{-1}, followed by 5WL, having a docking score of -12.63 kcal mol^{-1}, LC3 (-9.790), 5X2 (-8.860), Q0D (-7.090), 5X3 (6.650), and 70R (9.480) (Table S7). Based on the resolution, 5FC4 was selected as the reference, and Fig. 16 displays the docking pose of 5WL and **P1**. The selected compound **P1** formed hydrogen bonds with the amino acids Arg263 and Thr266. Also, it forms pi–pi interactions with Phe228, and pi–alkyl interactions with Ala227 and Met231 (Fig. 17A). These interactions suggest favourable binding of **P1** with the protein. In comparison, the 5WL formed hydrogen bonding interactions with amino acids Arg263 and Thr266, halogen bond interaction with Ala227, pi–pi interaction with Phe270 and His224, and pi–alkyl interaction with Phe228, Met231, and Leu267 (Fig. 17B). From the interaction analysis, the higher docking score and presence of interaction with important amino acids Arg263 and Thr266 suggest that the selected molecule **P1** possesses the capability to act as an anticancer compound.[43] To validate the docking outcome and study the functional impact of **P1** on cancer cell viability, the MTT assay was subsequently performed using MCF7 breast cancer cells, HeLa (cervical cancer cells) and WS1.

3.9. Cell viability analysis

3.9.1. MTT assay. To experimentally study the anticancer potential of the synthesized compound **P1**, the MTT assay was conducted on the MCF7 breast cancer cell line. Selection of MCF7 was made based on the overexpression of Mcl-1 enzyme in breast cancer.[44] This cell line provides a relevant model to assess the functional impact of molecule **P1** on the Mcl-1 protein. The MTT assay using MCF7 breast cancer cells reveals an IC_{50} value of 20 μM, which indicates moderate biological activity (Fig. 18A). **P1** showed dose-dependent cytotoxicity in cervical cancer cells (HeLa) in a similar fashion to that observed

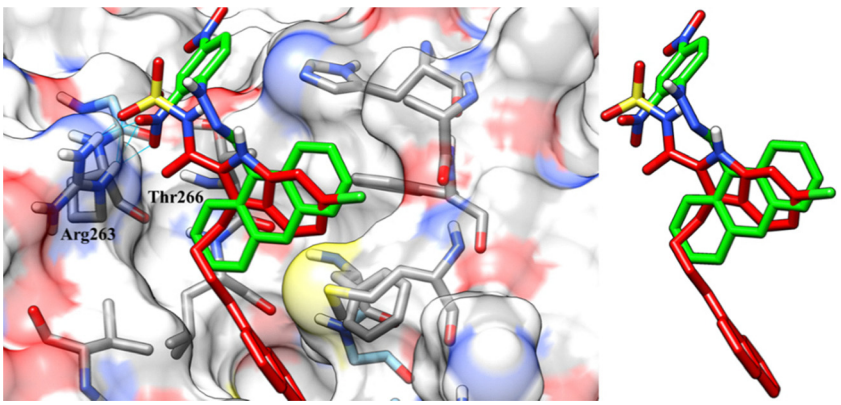

Fig. 16 Overlay of the docked molecule (**P1** green) and experimentally co-crystallized inhibitor (5WL red) within the binding domain of the Mcl-1 protein.

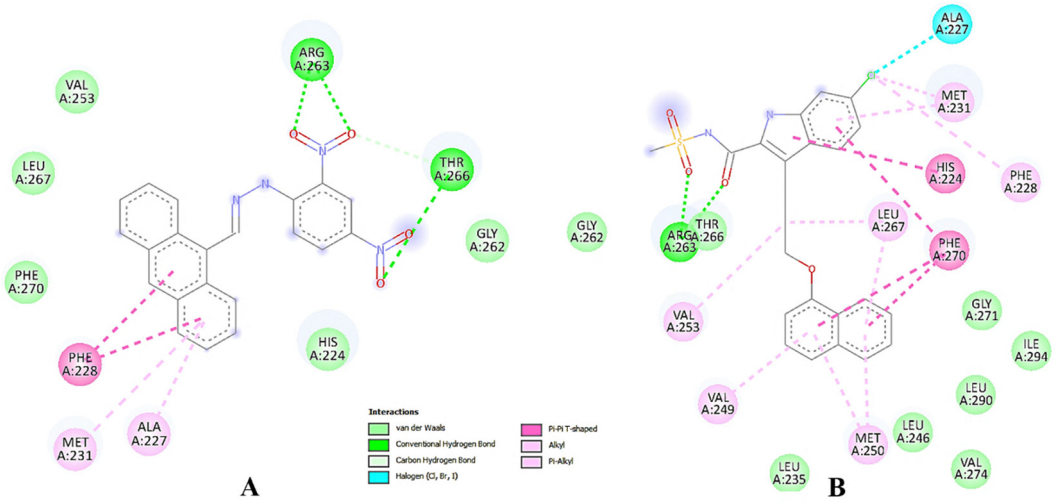

Fig. 17 2D interaction diagrams of (A) the selected molecule **P1** and (B) experimentally co-crystallised inhibitor 5WL docked within the binding domain of the Mcl-1 protein.

in MCF7 breast cancer cells. The IC_{50} value for **P1** in cervical cancer cells was 20 μM (Fig. 18B). In contrast, cisplatin demonstrated a much lower IC_{50} of 5.75 μM, suggesting stronger potency.[45] This comparison highlights that the new compound is less effective than cisplatin and may benefit from further optimization to enhance its activity. This result revealed that **P1** induces cytotoxicity similarly in different cancer cells. Further mechanism of action behind this phenomenon will be ascertained in our future studies. This concentration was used further for conducting the haemolytic assay.

3.9.2. Non-cytotoxic effect of P1 in normal fibroblast cells (WS1). As **P1** was found to be cytotoxic, the effect of **P1** in normal cells was calculated in normal fibroblast cells (WS1). The results showed that **P1** displayed almost no cytotoxicity on the normal fibroblast cells in the concentration range studied. Hence, it is clear that **P1** is less cytotoxic (almost nil) on normal cells, and hence it could be safe if used in normal cells for diagnostic or prognostic approaches (Fig. 18C).

3.9.3. Apoptotic assay by Annexin V–PI binding. The results of the effect of **P1** in Annexin V–PI binding assay revealed that there is a significant increase in the percentage of apoptotic cells in the treatment groups when compared to the control (Fig. 19).

From Fig. 19, it is observed that the percentage of live, apoptotic, and dead cells in untreated and 10 μM, 20 μM, and 30 μM treated groups was found to be 78 : 21 : 0.06; 19 : 80 : 0.12; 13 : 86 : 0.03 and 11 : 87 : 0.65, respectively, indicating a dose-dependent increase in the apoptosis levels on MCF7 cancer cells with **P1** treatment. The percentage increase in the early apoptotic cells on treatment with **P1** revealed that **P1** exhibits cytotoxicity in cancer cells in a programmed manner. The apoptosis exhibited by **P1** may be through the mitochondria-mediated pathway. Further mechanistic studies should be planned in the future to reveal this anticancer mechanism of action in cancer cells.

Arginine is needed for the multiplication of cancer cells like MCF7 and HeLa cells. Though arginine is not a cancer biomarker, it is an important amino acid involved in protein synthesis required for cancer cell progression. Increased arginine demand was seen in the tumor microenvironment, which was reported in many cancers. It is a precursor of nitric oxide, which is essential for the progression of many cancer cells. At the same time, arginine is needed for the functioning of immune cells, such as NK cells. NK cells destroy the cancer cells, and they inhibit the cancer cell progression. Hence, it is ironic to note that though arginine demand is high, the cells secrete arginine-inhibiting enzymes (arginases) in their microenvironment to control its utilisation by the cancer-fighting immune cells. Based on these facts, since our compound **P1** interacts with arginine and senses it, this could possibly be utilised in the development of novel diagnostics for cancer.[46,47]

Mcl-1 belongs to the family of Bcl2, a group of anti-apoptotic proteins. In the case of cancer progression, poor treatment response, and cancer cell resistance to therapies, high expression of Mcl-1 is observed. Hence, Mcl-1 plays a pivotal role in cancer; interaction of our novel compound **P1** with Mcl-1 protein could possibly contribute to new cancer diagnosis and therapeutic strategies.[48]

Heterocyclic ring compounds like pyrrole, pyrazole, quinoline, and indole act as Mcl-1 inhibitors. Many Mcl-1 inhibitors are currently in clinical trials to evaluate their potential as potent anticancer drugs in humans. To the best of our knowledge, no Mcl-1 inhibitor has been approved as an anticancer drug to date.[26,49] This gives us a compelling possibility to design compound **P1** as an anticancer agent.

3.9.4. Haemolysis assay. The *in vitro* biocompatibility of probe **P1**, both as a sensor and therapeutic agent, is important for its safe biomedical applications. Upon administration into the body, the compound first comes into contact with the circulatory system, particularly red blood cells, before reaching its target site. Hence, it becomes essential to evaluate its effects

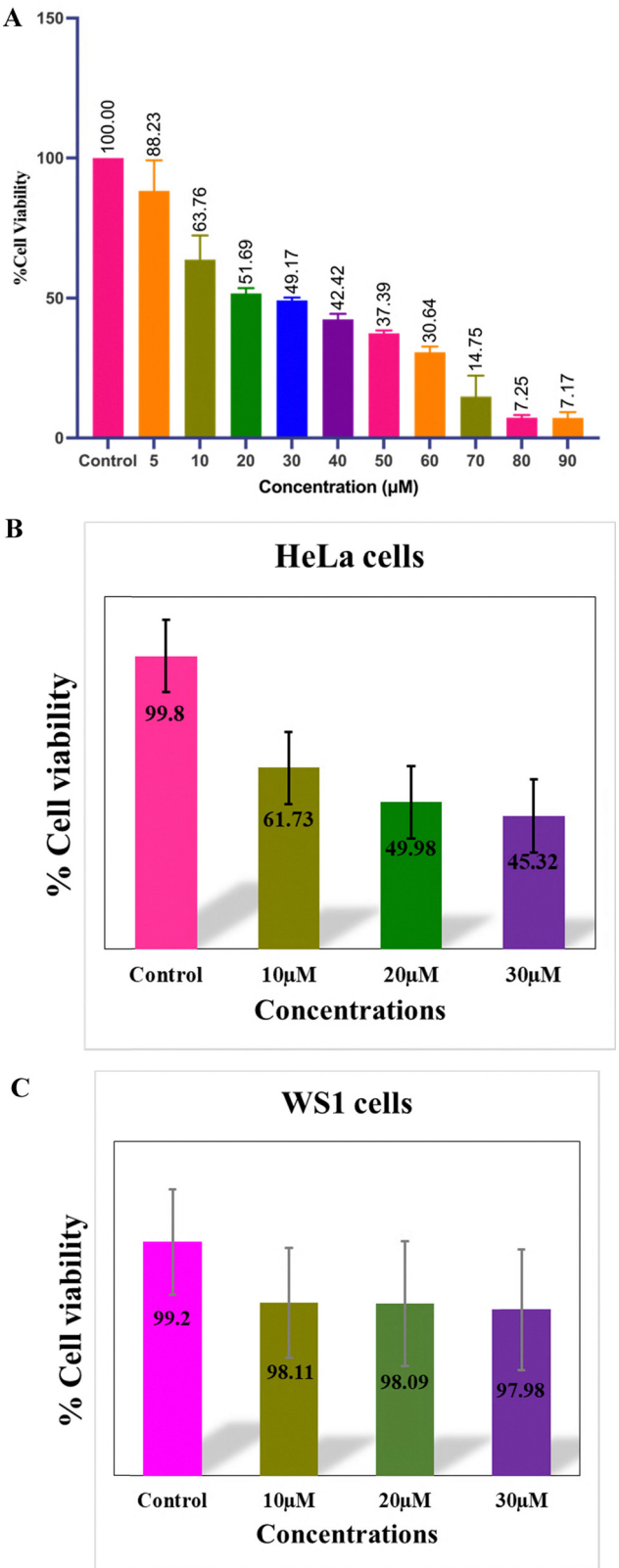

Fig. 18 (A) Effect of compound **P1** on the viability of MC7 breast cancer cells. (B) Effect of compound **P1** on the viability of HeLa cervical cancer cells. (C) Effect of compound **P1** on the viability of WS1 fibroblast cells.

on red blood cells to assess its safety for *in vivo* application. To asses this, a haemolysis assay was performed to examine the extent of red blood cell damage upon exposure to the synthesized compound (Fig. 20). **P1** was tested at various concentrations, and the results showed that **P1** accounted for no significant dose-dependent haemolysis up to 20 μM, in comparison to positive and negative control (PC and NC), respectively, indicating that **P1** is non-haemolytic and exhibits acceptable biocompatibility at biologically relevant concentrations. The data are summarized in Fig. 20. These findings support the potential for safe and systemic administration of **P1** in future therapeutic applications.[23,32] Following the confirmation of biocompatibility, molecular dynamics simulations were conducted to further evaluate the structural stability and interaction energy profile of the **P1**–Mcl-1 complex under physiological conditions.

3.10. Molecular dynamics simulations

Molecular dynamics simulations were conducted for 300 ns on each system, and plots like RMSD, RMSF, RoG, and H-bond and interaction energies were computed to evaluate the stability of the docked complex.

3.10.1. Root mean square deviation (RMSD). RMSD measures structural deviations of the protein backbone from the starting to final coordinates during the simulation, indicating structural stability. Lower RMSD values typically suggest a greater stability of the system. In this context, the RMSD for the protein–ligand complexes was assessed, as illustrated in Fig. 21. The mean RMSD values for 5FC4_5WL and 5FC4_**P1** were 0.200 ± 0.021 nm and 0.230 ± 0.015 nm, respectively. It was observed that the docked molecule exhibits a slightly higher RMSD value than the reference. Although **P1** possesses a high RMSD value, most of its deviation occurs only between 0.2 nm and 0.25 nm. In contrast, the 5WL deviation fluctuates between 0.15 nm and 0.225 nm, indicating a more variable deviation than **P1**. Therefore, the stable deviation of **P1** suggests greater stability than the reference 5WL.

3.10.2. Root mean square fluctuation (RMSF). RMSF analysis was conducted to assess the protein backbone's flexibility throughout the 300 ns molecular dynamics simulation run. The RMSF values indicate how much each residue varies from its average position throughout the simulations, offering insights into the stability and flexibility of particular areas within the protein structure. The average RMSF values of 5WL and **P1** were calculated to be 0.107 ± 0.053 nm and 0.097 ± 0.043 nm, respectively. As shown in Fig. 22, the residues of 5FC4 bound to 5WL exhibit greater fluctuation than those of **P1**. Therefore, the interaction of **P1** is stronger than that of 5WL, resulting in less deviation of the protein residues and suggesting stable behaviour compared to the reference ligand.

3.10.3. Radius of gyration (RoG). A 300 ns MD simulation was utilized to evaluate RoG, which helps examine the overall compactness and shape of the protein throughout the simulation. It assesses how the protein mass is distributed in relation to its centre of mass for each trajectory frame, comparing this with the hydrodynamic radius obtained from

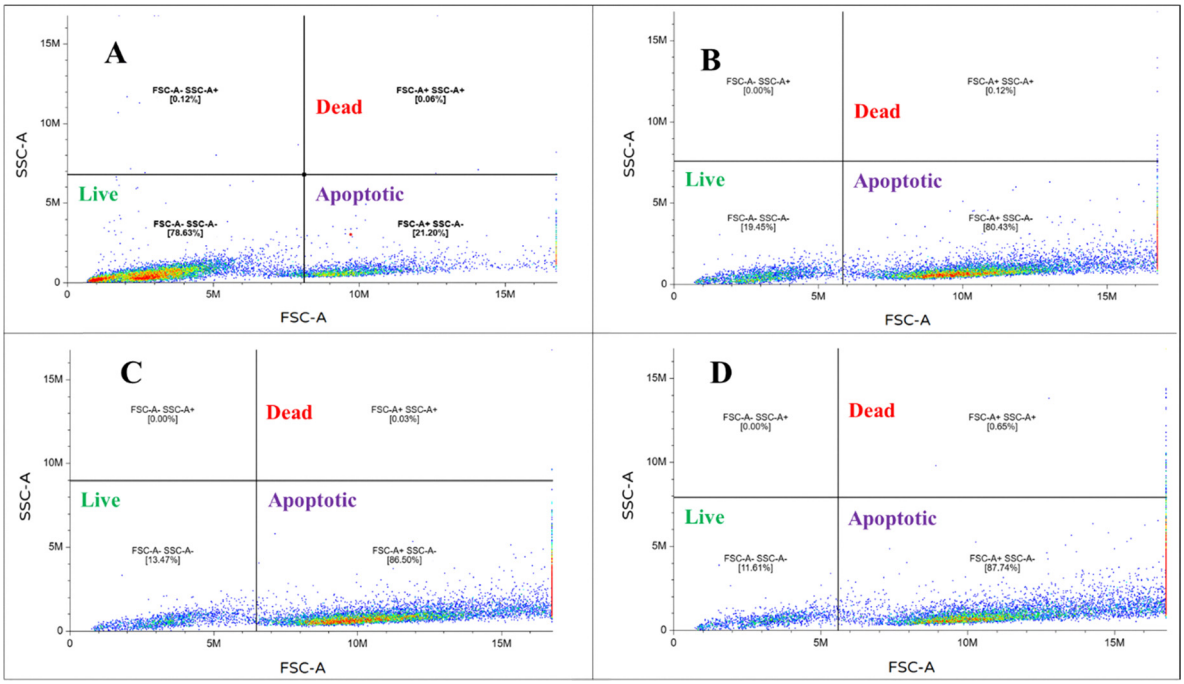

Fig. 19 Effect of compound **P1** on apoptosis of MCF7 cells. (A) Untreated cells; (B) 10 μM **P1**-treated, (C) 20 μM **P1**-treated, and (D) 30 μM **P1**-treated groups.

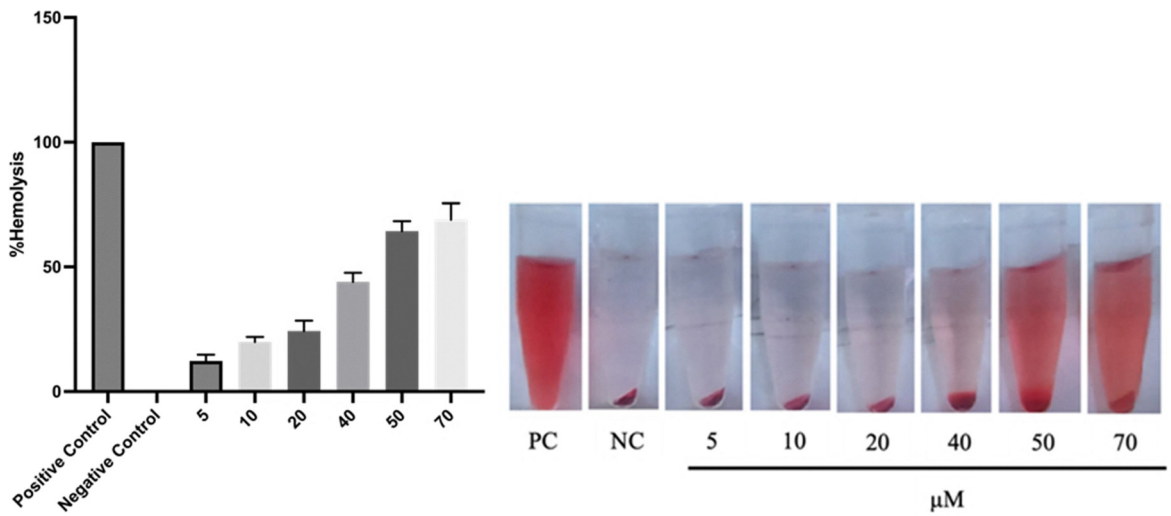

Fig. 20 Quantitative and visual analyses: percentage haemolysis induced by compound **P1** in human red blood cells (concentrations along the *x*-axis are in the μM range, PC: positive control and NC: negative control).

experiments. As shown in Fig. 23, the binding of **P1** with the protein results in a more compact and stable structure compared to that of 5WL. The average RoG values for 5WL and **P1** were found to be 1.446 ± 0.009 nm and 1.432 ± 0.009 nm, respectively.

3.10.4. Hydrogen bond (H-bond) interaction analysis. Investigating H-bonds is essential for studying their influence on the selectivity and stability of protein–ligand complexes. These bonds stabilize the ligand's attachment to the protein, affecting its stability and specificity. The number of H-bonds formed by the reference and docked molecules over 300 ns is shown in Fig. 24. The average number of H-bonds for 5WL and **P1** was 0.340 ± 0.641 and 0.293 ± 0.524, respectively. Fig. 24 shows that after 190 ns, **P1** establishes more hydrogen bonds within the protein's binding site, indicating a stronger interaction between **P1** and the protein.

3.10.5. Protein–ligand interaction energy. The analysis of interaction energy reveals the strength of ligand interactions

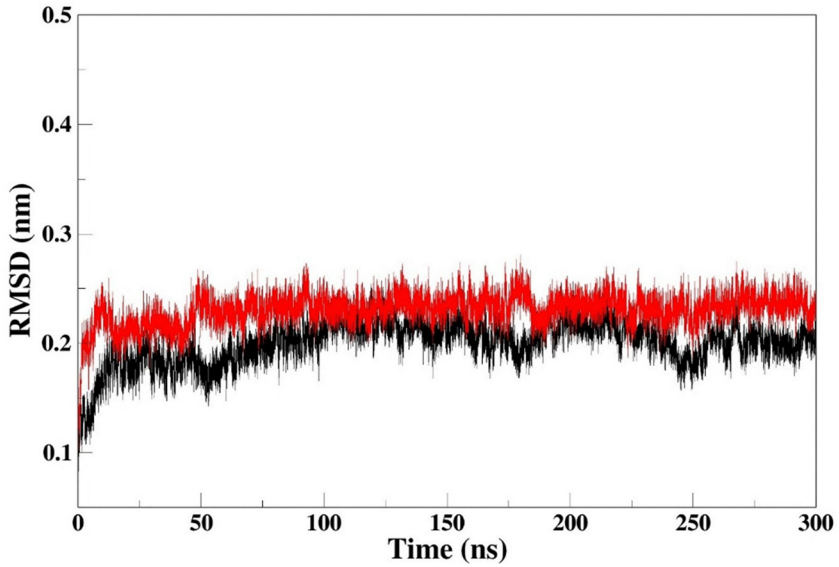

Fig. 21 RMSD plot of 5FC4 in complex with reference 5WL (black) and molecule **P1** (red) generated over a 300 ns time frame.

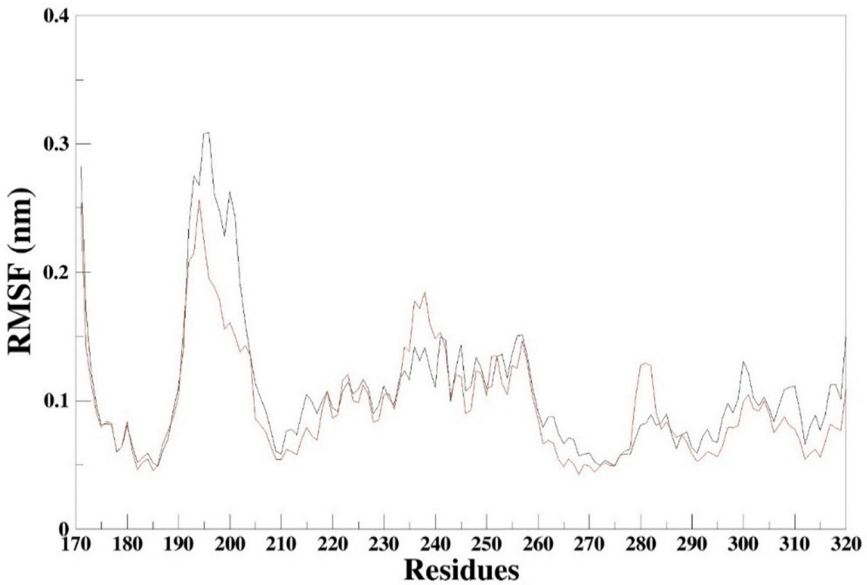

Fig. 22 RMSF plot of 5FC4 in complex with reference 5WL (black) and molecule **P1** (red) generated over a 300 ns time frame.

within the binding site of the protein. In this context, the calculations of non-bonded interactions (Coulombic energy) and bonded interactions (Lennard-Jones energy) are performed for both the reference (5FC4_5WL) and the docked compound (5FC4_**P1**). The average Coulombic energy for 5WL and PL1 was estimated to be -24.439 ± 26.622 kJ mol^{-1} and -29.717 ± 12.386 kJ mol^{-1}, respectively. Therefore, the non-bonded interaction of **P1** is slightly greater, indicating that the molecule exhibits a strong non-bonded interaction with the protein. As illustrated in Fig. 25A, **P1** exhibits unstable deviations up to 50 ns, followed by a linear deviation ranging from -25 kJ mol^{-1} to -75 kJ mol^{-1}. Meanwhile, 5WL shows more fluctuating deviations, which indicates the stable behaviour of **P1**. Furthermore, the Lennard-Jones energy was also calculated, and the mean values for 5WL and **P1** were -160.250 ± 21.123 kJ mol^{-1} and -150.02 ± 14.316 kJ mol^{-1}, respectively. Although the mean Lennard-Jones energy value of 5WL is higher than that of **P1**, this compound demonstrates a more stable interaction than the reference molecule. As shown in Fig. 25B, **P1** represents a smoother deviation, ranging between -130 kJ mol^{-1} and -180 kJ mol^{-1}, while 5WL does not exhibit the linear deviation seen in **P1**.

Overall, from the molecular dynamics simulations of the **P1**–Mcl-1 complex, the RMSD, RMSF, RoG, H-bond, and interaction analysis demonstrate the stability of **P1** at the active site of the enzyme under the physiological conditions.

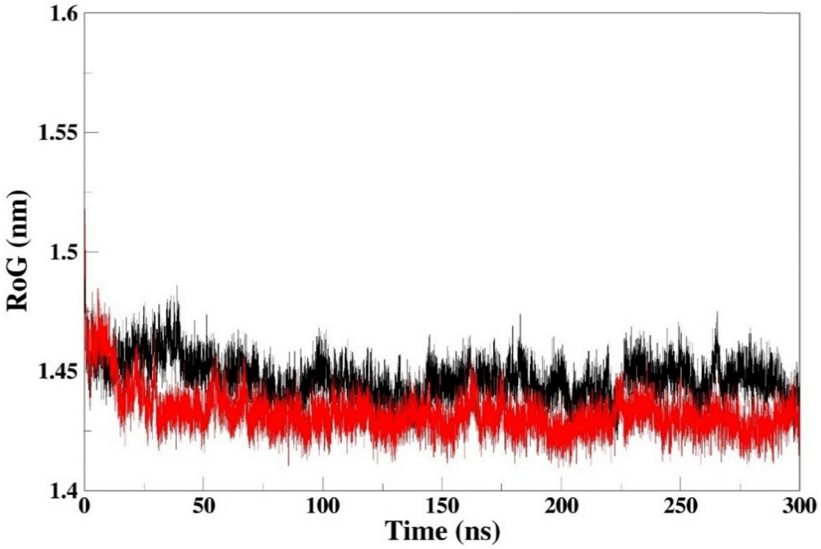

Fig. 23 RoG plot of 5FC4 in complex with reference 5WL (black) and molecule **P1** (red) generated over a 300 ns time frame.

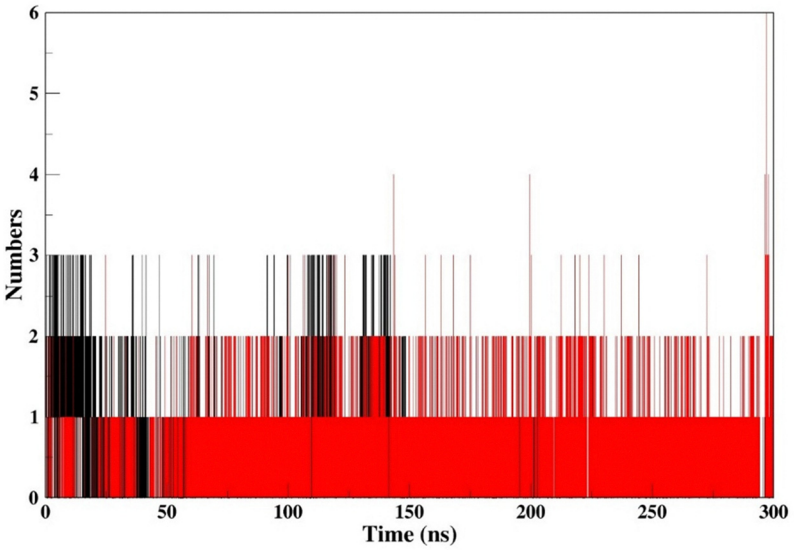

Fig. 24 H-bonds of 5FC4 in complex with reference 5WL (black) and molecule **P1** (red) generated over a 300 ns time frame.

4. Conclusions

In the current work, we have developed a highly efficient and selective colorimetric chemosensor for the detection of arginine, which offers distinct advantages such as rapid response time, operational simplicity, and a visible color change detectable by the naked eye. The sensor demonstrated excellent sensitivity, with a detection limit as low as 1.24 nM according to UV-Vis spectroscopy, and its practical applicability was validated through successful sensing in real biological and nutritional samples. The sensing mechanism has been thoroughly elucidated through ^{1}H NMR spectroscopy, which was supported by DFT calculations, providing deep insights into the interaction and binding selectivity toward arginine. In addition to its chemosensing capabilities, this molecule was also evaluated for its anticancer potential. Molecular docking studies using targets generated by Way2Drug software offered insights into the possible mechanisms underlying its anticancer activity, further strengthening its role as a multifunctional compound. Overall, the molecule interaction analysis of the compound reveals that the dinitrobenzene scaffold forms key hydrogen bonding interactions with Arg263 and Thr266. The residue Arg263 is considered a crucial amino acid present in the P2 pocket of the enzyme, responsible for forming a strong electrostatic interaction with the ligand.[43] The additional hydrogen bond with Thr266 stabilizes the compound at the binding site of the protein. Moreover, the anthracene moiety of the molecule forms a pi–pi interaction with the residue Phe228, which aligns well with the known Mcl-1 inhibitors. The outcome

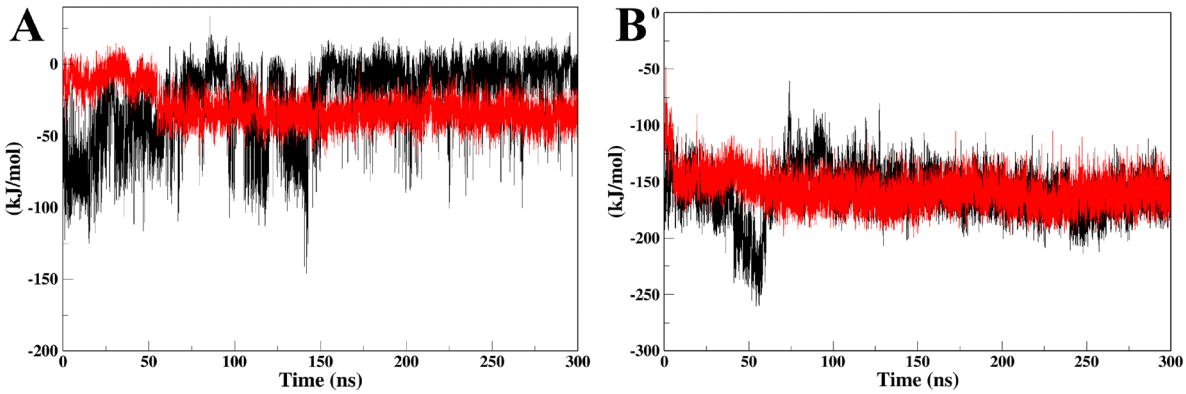

Fig. 25 Graphical representation of the protein–ligand interaction energy, where (A) represents Coulombic interaction energy and (B) represents Lennard-Jones interaction energy for reference 5WL (black) and molecule **P1** (red) generated over a 300 ns time frame.

suggests that our compound fits well at the binding site of the Mcl-1 enzyme, particularly in the P2 domain of the protein, thus mimicking the key interactions responsible for the high affinity of the molecules against the Mcl-1 enzyme.[43] Preliminary biological studies revealed promising anticancer effects at 20 μM concentration, indicating its dual functionality as both a sensor and a therapeutic agent. This dual application, both as a diagnostic chemosensor and a potential anticancer therapeutic agent, underscores its value in biomedical research. It is important to note that **P1** was found to be nontoxic in normal cells in the concentration range studied. The results of anticancer activity in the present study are promising. Furthermore, molecular dynamics simulations confirm the stable behaviour of the molecule **P1** in the binding pocket P2 of the enzyme, responsible for forming a strong electrostatic interaction with the ligand. Overall, this work not only presents a novel molecular tool for the selective detection of arginine but also opens avenues for future research on exploring its therapeutic potential, making it a compelling candidate for integrated sensing and treatment strategies.

Author contributions

Aayushi Joshi (experimental and DFT studies): data curation, formal analysis, investigation, and writing – original draft. Nikunjkumar Vagadiya (experimental studies): data curation, formal analysis, and investigation. Nisarg Rana (molecular docking and molecular dynamics simulations studies): data curation, formal analysis, and investigation. Giftson J. Senapathy (apoptosis and cytotoxicity assay): formal analysis and investigation. Rakesh Rawal (apoptosis): formal analysis and investigation. Helly Shah and Ranjitsinh Devkar (MTT and Haemolysis assay): formal analysis. Nandini Mukherjee: supervision, methodology, validation, and writing – review and editing. and Anu Manhas: supervision, methodology, validation, and writing – review and editing.

Conflicts of interest

The authors declared no conflict of interest.

Data availability

The authors confirm that all the supporting data and the findings of this study are included in the article and the attached supplementary information (SI). The supplementary information includes spectral data (mass spectrum, FT-IR, and NMR) for the synthesized probe (**P1**), ^{1}H NMR titration data with arginine, and molecular docking results with Mcl-1 protein. It also contains comparative analytical data for arginine-sensing probes, theoretical absorption calculations in different solvent environments, and optimized molecular coordinates of **P1**, analyte (**A1**), and product (**P1**–**A1**) from DFT calculations. Docking scores for known Mcl-1 inhibitors are also provided. See DOI: **https://doi.org/10.1039/d5ma00683j**.

Acknowledgements

Aayushi Joshi acknowledges financial support through the SHODH scheme (Grant number #2022015810), received from the Government of Gujarat. The corresponding authors and Nikunjkumar Vagadiya would like to acknowledge ORSP-PDEU (R&D/SRP/2021/019) for providing the funding, infrastructure and facilities to carry out this work.

References

1 A. A. Martíi Líndez and W. Reith, *Cell. Mol. Life Sci.*, 2021, **78**, 5303–5324.
2 X. Ma, M. Han, D. Li, S. Hu, K. R. Gilbreath, F. W. Bazer and G. Wu, *Amino Acids*, 2017, **49**, 957–964.
3 G. Wu and S. M. J. Morris, *Biochem. J.*, 1998, **336**(Pt 1), 1–17.
4 H. Wiesinger, *Prog. Neurobiol.*, 2001, **64**, 365–391.
5 M. Y. Zhu, A. Iyo, J. E. Piletz and S. Regunathan, *Biochim. Biophys. Acta, Gen. Subj.*, 2004, **1670**, 156–164.
6 K. E. J. Jungnickel, J. L. Parker and S. Newstead, *Nat. Commun.*, 2018, **9**, 1–12.
7 H. Al-Koussa, N. El Mais, H. Maalouf, R. Abi-Habib and M. El-Sibai, *Cancer Cell Int.*, 2020, **20**, 1–7.

8 Z. N. Ling, Y. F. Jiang, J. N. Ru, J. H. Lu, B. Ding and J. Wu, *Signal Transduction Targeted Ther.*, 2023, **8**, 345.
9 A. Mohammadi, S. Khoshsoroor and B. Khalili, *J. Photochem. Photobiol., A*, 2019, **384**, 112035.
10 B. M. C. Costa, A. A. Prado, T. C. Oliveira, L. P. Bressan, R. A. A. Munoz, A. D. Batista, J. A. F. da Silva and E. M. Richter, *Talanta*, 2019, **204**, 353–358.
11 G. Wu and C. J. Meininger, *Methods Enzymol.*, 2008, **440**, 177–189.
12 R. Bawa, N. Deswal, S. Negi, M. Dalela, A. Kumar and R. Kumar, *RSC Adv.*, 2022, **12**, 11942–11952.
13 A. Kastrati, F. Ostwald, A. Scalabre and K. M. Fromm, *Photochem*, 2023, **3**, 227–273.
14 D. Singh, I. Annan, S. Tyagi, V. Meena, S. Singh and R. Gupta, *J. Chem. Sci.*, 2023, **135**, 98.
15 M. Karimi Goftar, N. M. Kor and Z. M. Kor, *Int. J. Adv. Biol. Biomed. Res.*, 2014, **2**, 811–822.
16 J. A. Elliott, W. D. Wilson, R. G. Shea, J. A. Hartley, K. Reszka and J. W. Lown, *Anticancer Drug Des.*, 1989, **3**, 271–282.
17 R. Su, L. Dong, Y. Li, M. Wei, D. Horne and J. Chen, *Cancer Cell*, 2020, 79–96.
18 J. Huang, H. Zhao, X. Yu, Y. Limeng, C. Fan, P. Liao, B. Zhang, C. Li, G. Du, Q. Dong and C. Zeng, *Dyes Pigm.*, 2023, **217**, 111414.
19 B. Zhang, F. Zhou, X. Yu, P. Zhang, X. Sun, J. Su, C. Fan, W. Shu, Q. Dong and C. Zeng, *Food Chem.*, 2024, **455**, 139976.
20 X. Yu, B. Zhang, C. Fan, Q. Yan, S. Wang, H. Hu, Q. Dong, G. Du, Y. Gao and C. Zeng, *iScience*, 2022, **25**, 104964.
21 X. Yu, B. Zhang, P. Liao, J. Huang, C. Fan, H. Hu, Q. Dong, G. Du, Y. Gao and C. Zeng, *Dyes Pigm.*, 2022, **203**, 110339.
22 J. Huang, C. Li, P. Zhang, C. Fan, X. Yu, Q. Jiang, W. Chi, W. Shu, Q. Dong and C. Zeng, *Sens. Actuators, B*, 2025, **423**, 136861.
23 P. Nariya, F. Shukla, H. Vyas, R. Devkar and S. Thakore, *Synth. Commun.*, 2020, **50**, 1724–1735.
24 J. Leckenby, H. Li, K. Negus, M. Pickering, T. Adorno, M. Horkheimer, S. Dolnicar, A. Chapple, P. U. of P. P. Beck, A. (1967). Depression: Clinical, Experimental & Theoretical Aspects. Philadelphia, A. (2004): 161-9. Fenkçi IV, Maternal Fizyoloji. 'Çiçek MN, Ed.' Kadın Hastalıkları ve Doğum Bilgisi, Öncü Basımevi, R. C. Team, G. Payerle, C. H. S. and D. Turnbull, G. Bellingham, P. Peng, a Bruns, C. H. S. and D. Turnbull, S. Dolnicar, A. Chapple, T. Adorno, M. Horkheimer, K. Negus, M. Pickering, J. Leckenby, H. Li, A. (2004): 161-9. Fenkçi IV, Maternal Fizyoloji. 'Çiçek MN, Ed.' Kadın Hastalıkları ve Doğum Bilgisi, Öncü Basımevi, 1995. MILLS, Anthony F. Transferencia de calor. Irwin, G. Payerle and R. C. Team, *Why We Need J. Interact. Advert.*, 2014, 3, 45.
25 W. Humphrey, A. Dalke and K. Schulten, *J. Mol. Graphics*, 1996, **14**, 33–38.
26 V. Sharma and A. Kumar, *Bioorg. Chem.*, 2025, **156**, 108211.
27 M. Rarey, B. Kramer, T. Lengauer and G. Klebe, *J. Mol. Biol.*, 1996, **261**, 470–489.
28 2023 SeeSAR version 13.1.1BioSolveIT GmbH, Sankt Augustin, Germany.
29 H.-J. Böhm, *J. Comput. Aided. Mol. Des.*, 1994, **8**, 243–256.
30 H. S. Vyas, R. N. Jadeja, A. Vohra, K. K. Upadhyay, M. C. Thounaojam, M. Bartoli and R. V. Devkar, *Antioxidants*, 2023, **12**, 997.
31 G. J. Senapathy, B. P. George and H. Abrahamse, *Molecules*, 2020, 25.
32 J. Y. Soni, S. Sanghvi, R. V. Devkar and S. Thakore, *RSC Adv.*, 2015, **5**, 82112–82120.
33 M. J. Abraham, T. Murtola, R. Schulz, S. Páll, J. C. Smith, B. Hess and E. Lindah, *SoftwareX*, 2015, **1–2**, 19–25.
34 K. Lindorff-Larsen, S. Piana, K. Palmo, P. Maragakis, J. L. Klepeis, R. O. Dror and D. E. Shaw, *Proteins Struct. Funct. Bioinform.*, 2010, **78**, 1950–1958.
35 A. W. Sousa Da Silva and W. F. Vranken, *BMC Res. Notes*, 2012, **5**, 1–8.
36 H. J. C. Berendsen, J. P. M. Postma, W. F. Van Gunsteren, A. Dinola and J. R. Haak, *J. Chem. Phys.*, 1984, **81**, 3684–3690.
37 M. Parrinello and A. Rahman, *Phys. Rev. Lett.*, 1980, **45**, 1196–1199.
38 T. Darden, D. York and L. Pedersen, *J. Chem. Phys.*, 1993, **98**, 10089–10092.
39 B. Hess, H. Bekker, H. J. C. Berendsen and J. G. E. M. Fraaije, *J. Comput. Chem.*, 1997, **18**, 1463–1472.
40 G. Lu, X. Ju, X. Chen, W. Pei and Z. Cai, *J. Syst. Softw.*, 2024, **212**, 112031.
41 P. E. Hansen, *Molecules*, 2021, **26**, 2409.
42 J. Contreras-García, W. Yang and E. R. Johnson, *J. Phys. Chem. A*, 2011, **115**, 12983–12990.
43 N. F. Pelz, Z. Bian, B. Zhao, S. Shaw, J. C. Tarr, J. Belmar, C. Gregg, D. M. V. Camper, C. M. Goodwin, A. L. Arnold, J. L. Sensintaffar, A. Friberg, O. W. Rossanese, T. Lee, E. T. Olejniczak and S. W. Fesik, *J. Med. Chem.*, 2016, **59**, 2054–2066.
44 K. J. Campbell, S. M. Mason, M. L. Winder, R. B. E. Willemsen, C. Cloix, H. Lawson, N. Rooney, S. Dhayade, A. H. Sims, K. Blyth and S. W. G. Tait, *Cell Death Differ.*, 2021, **28**, 2589–2600.
45 J. O. Suberu, I. Romero-Canelón, N. Sullivan, A. A. Lapkin and G. C. Barker, *ChemMedChem*, 2014, **9**, 2791–2797.
46 S. Zou, X. Wang, P. Liu, C. Ke and S. Xu, *Biomed. Pharmacother.*, 2019, **118**, 109210.
47 D. Bai, Y. Zhou, L. Jing, C. Guo and Q. Yang, *Immune Netw.*, 2025, **25**, e30.
48 M. Vogler, Y. Braun, V. M. Smith, M.-A. Westhoff, R. S. Pereira, N. M. Pieper, M. Anders, M. Callens, T. Vervliet, M. Abbas, S. Macip, R. Schmid, G. Bultynck and M. J. S. Dyer, *Signal Transduction Targeted Ther.*, 2025, **10**, 91.
49 N. P. Shukla and G. J. Senapathy, *Crit. Rev. Ther. Drug Carrier Syst.*, 2025, **42**, 89–118.